



HAL
open science

First insights to the seismic response of the fractured Carboniferous limestone reservoir at the Balmatt geothermal doublet (Belgium)

Jannes Kinscher, Matsen Broothaers, Jean Schmittbuhl, Francesca de Santis,
Ben Laenen, Emmanuelle Klein

► To cite this version:

Jannes Kinscher, Matsen Broothaers, Jean Schmittbuhl, Francesca de Santis, Ben Laenen, et al. First insights to the seismic response of the fractured Carboniferous limestone reservoir at the Balmatt geothermal doublet (Belgium). *Geothermics*, 2023, 107, pp.102585. 10.1016/j.geothermics.2022.102585 . ineris-03854360

HAL Id: ineris-03854360

<https://ineris.hal.science/ineris-03854360>

Submitted on 5 Dec 2022

HAL is a multi-disciplinary open access archive for the deposit and dissemination of scientific research documents, whether they are published or not. The documents may come from teaching and research institutions in France or abroad, or from public or private research centers.

L'archive ouverte pluridisciplinaire **HAL**, est destinée au dépôt et à la diffusion de documents scientifiques de niveau recherche, publiés ou non, émanant des établissements d'enseignement et de recherche français ou étrangers, des laboratoires publics ou privés.

First insights to the seismic response of the fractured Carboniferous limestone reservoir at the Balmatt geothermal doublet (Belgium)

Jannes L. Kinscher^{1*}, Matsen Broothaers², Jean Schmittbuhl³, Francesca de Santis¹, Ben Laenen², Emmanuelle Klein¹

1 Ineris - L'Institut national de l'environnement industriel et des risques Campus ARTEM, 92 rue Sergent Blandan, BP 14234, F-54042 Nancy cedex, France

2 VITO – Vlaamse Instelling voor Technologisch Onderzoek, Boeretang 200, 2400 Mol, Belgium

3 EOST, ITES, CNRS, Université de Strasbourg Strasbourg, France,

*Corresponding author. E-mail address: Jannes-L.KINSCHER@ineris.fr

Abstract

We present the main features of the geothermal production history between 2018 and 2019 at the Balmatt geothermal doublet (3-4 km depth), located in Mol in northern Belgium, and the recorded seismic data set which represents the first return of experience on the seismic response of the fractured Lower Carboniferous Limestone reservoir in the Campine Basin to fluid injection. The study has been motivated by the occurrence of a felt $M_L = 2.2$ event leading to the temporal suspension of the project due to a red-light status of the traffic light system. Even though the seismic data set is comparatively limited ($M_c \sim 0.6$), thanks to a precise analysis of the seismic source features, we derive a new conceptual structural reservoir model that includes a hidden fault zone not seen during the exploration and provides new constraints on the main hydro-mechanic processes involved in the triggering of seismicity and seismic hazard.

Highlights

- Geothermal exploration of the fractured Carboniferous limestone reservoir in Belgium

- Evaluation of network performance and seismic reservoir propagation characteristics and waveform-based source analysis.
- Evidence for stimulation of pre-existing fault zone oriented preferentially to the maximum horizontal stress
- Evidence for fracture dominated reservoir and dominance of direct pressure effect consistent with Mohr-Coulomb failure criterium.
- Discussion on seismic moment release vs injected volume and M_{Max} prediction models

Keywords: Fluid-injection induced seismicity, Geothermal limestone reservoir, Seismic hazard

1 Introduction

Geothermal energy production in Europe has gained in importance with the energy system transition. The recent gas crisis has particularly exacerbated this need to develop the use of the subsurface for exploiting carbon free energy sources despite the challenge of controlling the seismic risk, as e.g. shown by the recent case of Strasbourg (Schmittbuhl et al., 2021), which led to the definitive suspension of several projects (e.g Giardini, 2009; Huenges and Ledru, 2011; Lee et al., 2019; Mignan et al., 2017; Moeck et al 2015). Many attempts have been made to predict and control seismic hazard (e.g. Gaucher et al, 2015), but unexpected triggering of larger events due to the highly complex rock-fluid interaction can apparently rarely be completely excluded (e.g. Ellsworth et al., 2019). Some progress in the prediction of seismicity and its maximum magnitude M_{max} has been made by interpreting trends between production and seismic parameters (e.g. seismic moment release vs injected volume) highlighted thanks to the analyses of shared data sets from deep fluid injection projects (e.g. Bentz et al., 2020; Galis et al., 2017; McGarr, 2014; McGarr and Barbour, 2018; Shapiro et al., 2007, 2010; Van der Elst et al., 2016 ; Zang et al., 2014).

We present a new case study from the geothermal plant at the Balmatt brownfield site in Mol-Donk, Belgium (here after called Balmatt), which represents the first return of experience on the seismic response of a fractured Lower Carboniferous limestone reservoir to fluid injection. The fractured and karstified limestones and dolostones of the Lower Carboniferous Limestone

Group has been marked as a potential deep geothermal reservoir in northern Belgium (Berckmans and Vandenberghe, 1998; Vandenberghe and Bouckaert, 1980, Vandenberghe, 1991), The amount of extractable heat was estimated at 13×10^9 GJ (GEOHEAT-APP, 2014). In 2009 the Flemish Institute for Technological Research (VITO) started to explore the potential development of a geothermal cogeneration plant at Balmatt. The geothermal plant offered the perspective to be easily connected to the existing heat network around the offices of VITO and adjacent companies (Bos and Laenen, 2017; Broothaers et al., 2019).

An active seismic acquisition survey was carried out in 2010, and 3 deep geothermal wells (GT-01@3200m, GT-02@3804m, and GT-03@4200m) were drilled between 2015 and 2018 (Figure 1). The wells confirmed the presence of a geothermal reservoir in the Lower Carboniferous limestones at 3200 - 3600 m depth. Formation temperature is in the range of 138 - 142°C. In addition, two NW-SE striking main fault structures were deduced from the data, called the Beringen and the Retie fault. From December 2018 until June 2019 several circulation test phases were initiated on wells GT-01 and GT-02, with injection in between both main faults. During the final and longest test phase in June 2019, 15,600 m³ of water were produced over a period of 10 days. To mitigate the associated seismic hazard and risk, VITO operated a microseismic monitoring network (Figure 1), involving deep borehole sensors between 200 m and 600 m depth. During monitoring, around 250 seismic events with magnitudes $-1 < M_L < 2.2$ were detected between December 2018 and June 2019. The strongest event occurred on the 23rd of June 2019 at 17:30 UTC (here after called “Jun-M2.2-event”). The event was felt by the population in the nearby towns of Dessel and Mol and triggered a red-light status of the local Traffic Light System (TLS) and a temporal suspension of geothermal production.

The following study provides new insights into the Balmatt geothermal reservoir configuration and contributes to a better understanding of its geothermal potential and associated seismic hazard. Even though the seismic data set is limited due to an unexpected low detection performance of the network (Section 2.3), we derive a conceptual structural reservoir model by means of careful evaluation of seismic reservoir propagation characteristics and wave form based source analysis (e.g. multiplet analysis, relocation, and determination of source parameters and mechanisms) optimized to confront the limited number of events and stations which impeded the simple application of standard procedures (Section 3). Based on the conceptual model (Section 4), we provide constraints on the hydraulic reservoir properties and

discuss the main hydro-mechanic processes involved in the triggering of seismicity (Section 5) and its implication on seismic hazard (Section 6). One important question addressed in terms of seismic hazard, is the potential generation of larger seismic events on the Beringen and Retie faults and their potential impact on the SCK-CEN nuclear research centre located at a few kilometres from the site (e.g. Vanneste et al., 2019). We furthermore discuss the most popular physical and probabilistic models promoting an apparent scaling relationship between the seismic moment release (M_{max}) and the total injected volume in the context of the seismic hazard at Balmatt and the prediction of the Jun-M2.2-event.

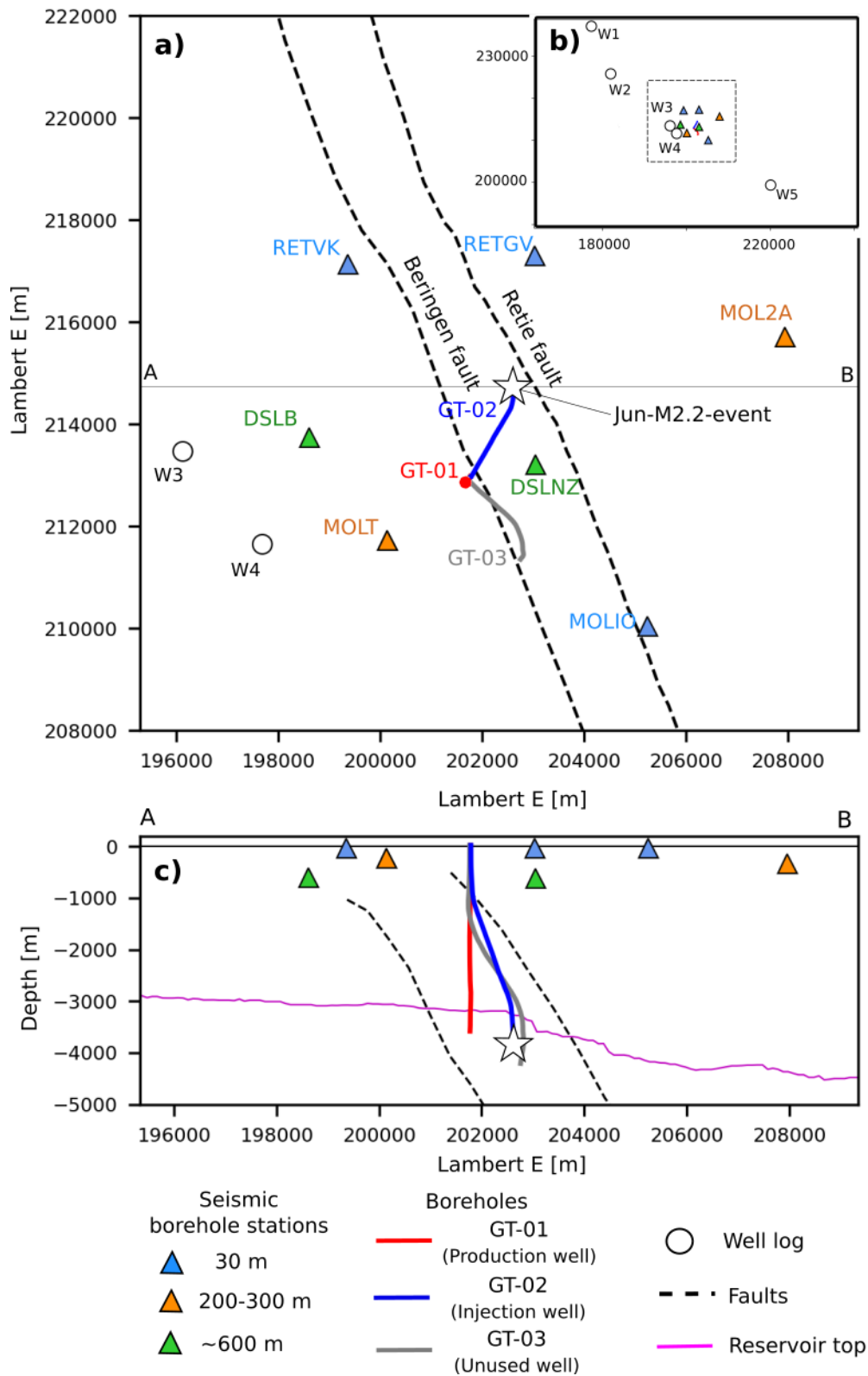


Figure 1: Overview of the Balmatt geothermal doublet site. a) (top view), c) (depth section) of the geothermal well configuration, seismic monitoring network, the Jun-M2.2-event (white star) (locations are taken here from the initial monitoring catalogue, see Section 2.1 and 3.2) and the main faults from the reservoir model; note that faults in c) are shown along profile A-B in a) corresponding to the Y coordinates of the Jun-M2.2-event. b) Outer zoom around Balmatt site to show locations of boreholes with well log information used for construction and evaluation of the velocity model in Section 3.1. c) The reservoir top in pink corresponds to the top of the Carboniferous limestones

2 Study site and data

2.1 Seismic network and monitoring

Seismic data were recorded by the microseismic network completed in December 2018 which included a total of seven borehole sensors with two at a depth of ~600 m, at the top of the Cretaceous chalk (DSLNB and DSLNZ), two at ~ 300 m (MOLT and MOL2A) and three at 30 m (RETVK, RETGV, MOLIO) depths (Figure 1). Borehole sensors (of type Guralp 3TB and IESE F86) provided a broadband response (respectively 10 sec or 40 sec sensors) except for the 2 Hz short period sensors (of type IESE G88) of stations DSLNZ and MOL2A. Stations DSLNB and MOLT were operated by the Royal Observatory of Belgium (ROB) and installed before 2016 by NIRAS/ONDRAF in the context of the cAt project. Data from these public stations were fully available for monitoring during well testing in 2016 and 2018, and afterwards during the circulation tests. Seismic monitoring was performed in real time by DMT GmbH on behalf of VITO and provided event detections, locations and magnitude estimates, i.e. the input data for the TLS, accessible in near real time on a public webpage.

Event detection was based on a classical STA/LTA detection function with a short-term average (STA) window of 0.01 s and long-term average (LTA) window of 8 s (pers. comm. with DMT). An event detection was triggered when 4 stations exceeded a threshold of STA/LTA ratio = 6 within a time window of 5 s. Locations were obtained by means of a station-corrected 1D velocity model constructed by assuming that the first recorded event (following the first circulation phase P1; see following Section 3 and Figure 2) is located at the injection well. Local magnitudes were estimated using the approach of Bormann and Dewey (2012) and then later corrected to be consistent with local magnitude estimates using the national seismological

network of the ROB. For the following analysis we used the full monitoring catalogue of seismic events recorded in 2018 and 2019, including event detection and magnitudes. As shown later in Section 3.1, event locations were revised by means of a wave form-based evaluation of the velocity model.

2.2 Overview of fluid injection and seismic data

The first (production) well GT-01 was drilled and completed in January 2016 targeting the Beringen fault (Bos and Laenen, 2017; Broothaers et al., 2019, 2021) (Figure 1). It reached the limestone reservoir at 3200 m TVD (True Vertical Depth). Total depth of the well is 3610 m. The production tests pointed to a productivity index of 4 – 5 m³/hr/bar (i.e. 1.1-1.4 l/s/bar), with a production temperature of up to 128°C. A second well, GT-02, was drilled for injection and reached 3804 m TVD with an open hole (slotted liner) section from around 3300 m TVD. An acid stimulation job was carried out in three steps, each spotting 30 m³ of a 15% HCl solution at different positions in the reservoir section. An initial short injection test (2200 m³) was followed later by a second extended injection test in September 2016 (almost 9000 m³) where the well-head pressure rose to almost 120 bar. The extended test revealed a much lower injectivity index of 1.5 – 2 m³/hr/bar (i.e. 0.4-0.5 l/s/bar), possibly related to the absence of highly permeable fault structures. Testing triggered the first measurable seismic response, which was recorded by the relatively distant stations DSLB and MOLT (Lecocq and Camelbeeck, 2019, Appendix A), the only stations available in the area at that time.

A second production well, namely GT-03, was then drilled in late 2017 to early 2018 crossing the entire Lower Carboniferous and exploring the underlying Devonian sandstones at 4200 m TVD. The well was deviated to the Southeast but targeting the same faulted zone as GT-01, the Beringen fault. Productivity of this well turned out to be low such that well was not used. Water was subsequently produced only from GT-01 (Broothaers et al., 2019, 2021). Circulation tests with injection at GT-02 and production at GT-01 were initiated in December 2018 following the construction of the surface installations, connection to the heating network and completion of the seismic monitoring network (Figure 2). The different circulation test phases can be summarized in 3 main stages with distinct seismic responses, involving two circulation test phases in December 2018 – January 2019 (P1) and March to April 2019 (P2) and a production phase in May – June 2019 (P3).

The first main stage P1 included three successive circulation tests (one of 3-days, P1.1, and two of 1-2 days, P1.2 and P1.3), reaching well-head pressures close to 100 bar in GT-02 (Figure 2a). This was followed one month later by a 3-day injection test reaching well-head pressures of almost 110 bar (P1.4). All tests were accompanied by several tens of recorded seismic events while circulation and during the shut-in phases. The strongest event occurred on the 18th of January 2019 at 08:24 UTC with a magnitude of $M_L = 1.8$ (here after called “Jan-M1.8-event”). This event is one of the key events in the following analysis, since all seismic sensors were operational at this period, and all recorded seismograms were associated with high signal to noise ratios. Another particularity of stage P1 is the occurrence of very late post-injection seismic activity more than a month after shut-in of tests P1.3 and P1.4 (see question marks in Figure 2a).

The second main stage P2 involved three shorter 2-day circulation phases (P2.1, P2.2 and P2.3) conducted in monthly intervals where maximum well-head pressures reached around 100 bar at GT-02 (Figure 2b). Apart from some few small events directly following the shut-in of the two first tests, no significant seismic activity was observed during P2.

The final circulation test stage P3 comprised three ‘short-term’ 2 – 3 day circulation tests (P3.1, P3.2 and P3.3) within a period of 16 days in May and a 10 days “long-term” circulation test in June (P3.4). Stage P3 was accompanied by significant seismic activity (Figure 2c). In the second and third short-term tests (P3.2 and P3.3), the number of recorded seismic events was comparable to tests in P1.1-3 but without the occurrences of any larger $M_L > 1$ event. More than a hundred seismic events, including six events of $M_L > 1$ were recorded in the final long-term circulation P3.4, while the onset in seismic activity is characterized by an apparent delay from injection start, which is also observed in P1. After 10 days the circulation had to be stopped abruptly due to a power break. Three days later, the occurrence of the Jun-M2.2-event causing a red alert status of the TLS due to exceedance of a threshold in the Peak Ground Velocity (PGV) of 1 mm/s. At that time, the plant was not in operation.

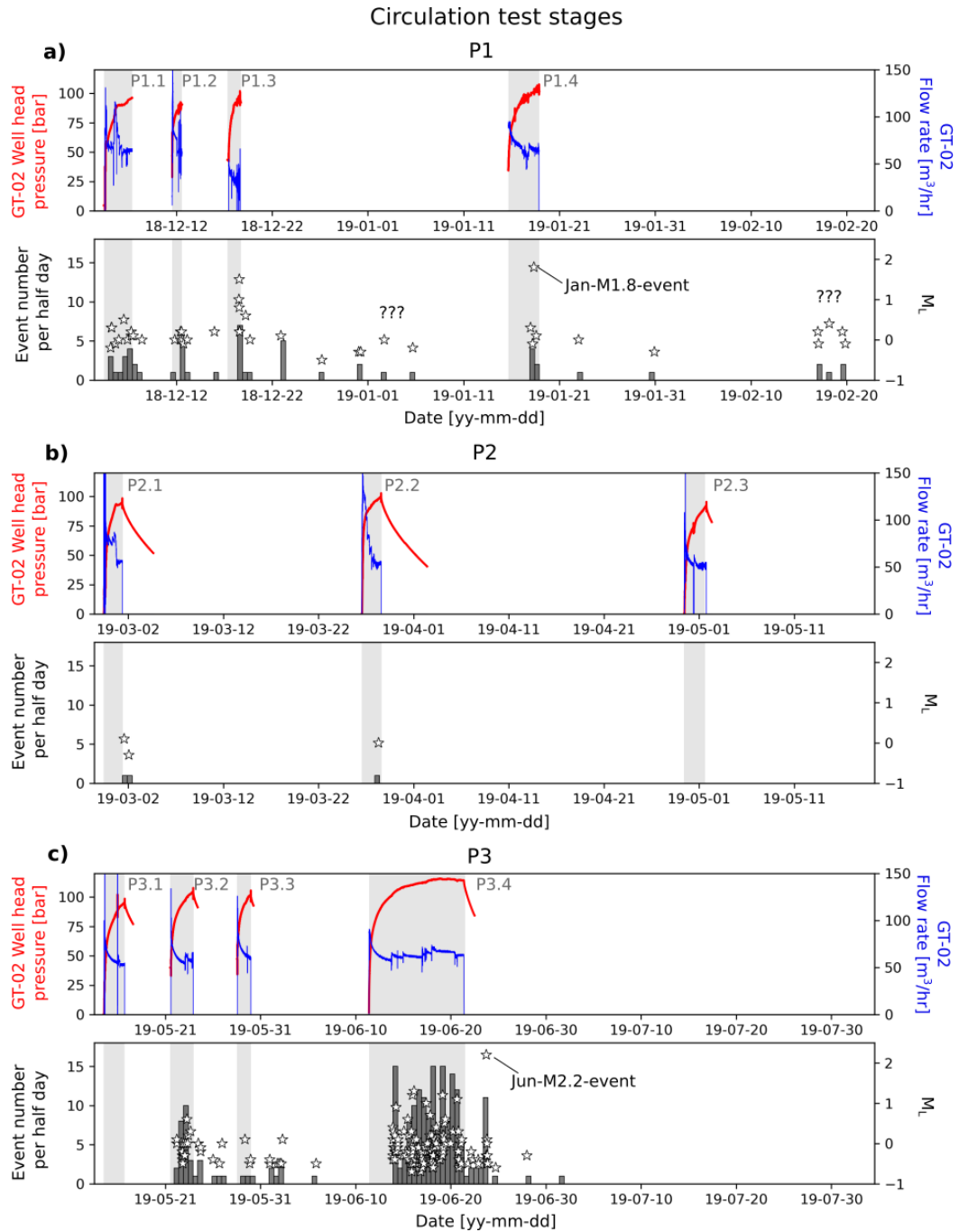


Figure 2: General overview of the circulation tests P1 a), P2 b) and P3 c) at GT-01 and 02 conducted in 2018 and 2019 (grey shaded areas mark the periods of production or injection) and the corresponding seismic response recorded by the monitoring network (Section 2.1) (grey bars and white stars); question marks in a) mark the occurrence of very late post-injection seismic activities.

2.3 Seismic data quality and limitation and network performance

Despite the relative short distances between the seismic stations and the injection area, the recorded event number appears low compared to other geothermal experiments (usually thousands of events instead of some hundred) which suggest that small magnitude events are missing. The main reason for the apparent limited network detection capacity is seen in the high background noise level of the closest 600 m deep borehole DSLNZ station (at ~ 1 km epicentral distance to the injection area) in combination with the applied standard amplitude-based detection routine. High background noise level is related to machinery noise coming from a nearby factory building. Noise level is estimated five to ten times higher compared to the highest performing stations, namely station DSLB (at 600 m depth) and MOL2 (at ~300 m depth), which are located at ~ 5 km and 6 km away from the injection well (Kinscher 2020a). The resulting detection capacity by DSLNZ is comparable to the one of the distant near-surface stations RETVK and RETGV located at 5 km and 4 km from the injection area, respectively. We also need to emphasize here that station MOLIO had to be totally excluded from the following analysis since seismograms were heavily polluted by a nearby wind turbine.

In order to assess the resulting network detection performance (for location performance see Section 3.2) we examined the magnitude of completeness M_c from the Gutenberg-Richter distribution of the entire seismic catalogue for stages P1-3 (Figure 3). First, we used the completeness model by Ogata and Katsura (1993) and fitted the observed magnitude-frequency distribution to synthetic catalogues generated by the combination of the Gutenberg-Richter relationship (assumed with b -value = 1) and a detection probability function (Figure 3a). From the best fitting model, we estimate that $M_c = 0.6$ (in local magnitude M_L) which corresponds to the lower magnitude from which the seismic catalogue is to 99% complete. Secondly, we followed the approach by Wiemer and Wyss (2000) and Cao and Gao (2002) and analysed the fluctuation of the b -value estimated from the maximum likelihood approach (Aki, 1965) for different M_c (Figure 3b). In the results, we observe apparent (even though not fully convincing) stability in the b -value around 0.8 for $M_c \geq 0.6$, which is in general agreement with the previous result, when accounting for uncertainties in b -value estimation. Similar estimates on M_c has been also found from simulations based on synthetic seismograms (Coutant, 1990) and observed background noise (absolute level measured from seismograms and added as gaussian white noise to the synthetics) and the monitoring specific detection

routines (Section 2.1), where we considered M_c to be the minimum magnitude at which an event is detectable and locatable (requires detection by at least 3 stations) within the area around the injection well (Kinscher 2020a).

The found magnitude of completeness of $M_c \sim 0.6$ explains the apparent lack of small magnitude events and likely results from the high background noise level of station DSLNZ. As a result of this limited detection capacity, the estimation of the b-value seems to be related to significant uncertainties, what questions the possibility of reliable probabilistic hazard assessment using the present network and station characteristics. It is well known that small changes in the b-value imply significant changes in the predicted number of future larger magnitude event occurrences. As shown from the completeness model, the b-value seems to lie generally around 1 (Figure 3a), while uncertainties are in the order of at least 0.2 (Figure 3b) as a result of the statistically low sample number. From our model we can show that the change in b-value 0.2 may imply a change in the number of predicted larger $M_L = 3$ and $M_L = 4$ events by a factor of around 4 and 7, respectively, which is not usable for reliable hazard assessment.

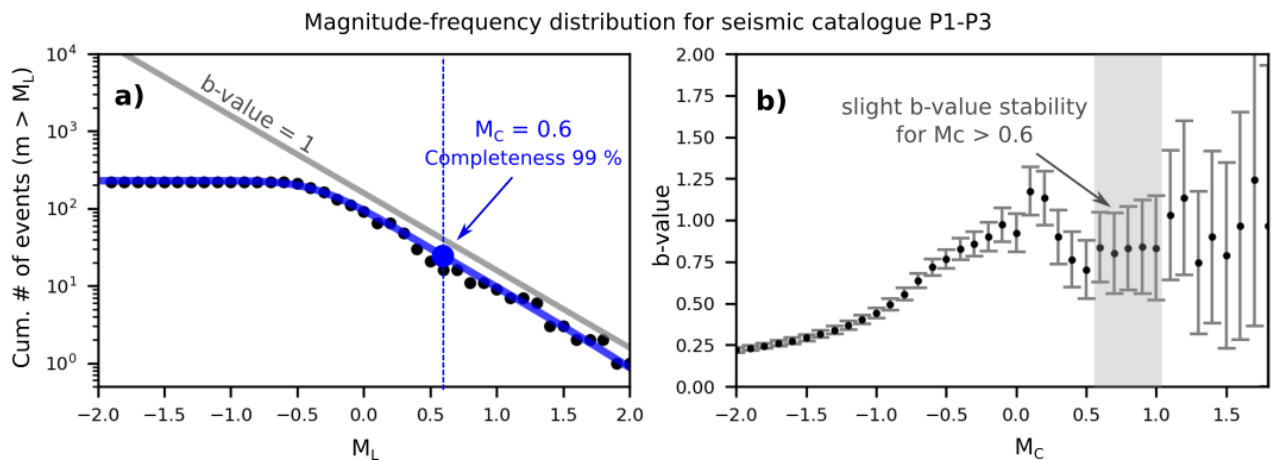


Figure 3: Estimation of magnitude of completeness M_c using probabilistic analysis on frequency-magnitude distribution for the seismic catalogue recorded from P1-3. a) Gutenberg Richter distribution and an the best fitting completeness model (blue line) based on the detection probability function by Ogata and Katsura (1993) $q(m) =$

$1/\sqrt{2\pi\sigma} \int_{-\infty}^m e^{-(x-\mu)^2/2\sigma^2} dx$, where μ is the magnitude at which 50% of the seismic events are detected and σ the speediness at which the complete detection capability is reached, here

estimated with 0.2 and 0.35, respectively. The found $M_c = 0.6$ corresponds to the magnitude where the catalogue is to 99% complete (blue point and dashed blue line); b) b-value estimations as a function of assumed M_c when applying the maximum likelihood approach by Aki (1965) with uncertainties (error bars) estimated by $\sigma = b/\sqrt{N}$, where N is the event number used to calculate b .

3 Method and results

3.1 Characterization of the velocity model

Direct measurements of seismic velocities and of the structure of the propagation medium are available from well logs and Vertical Seismic Profiling (VSP) data sets obtained at wells GT-01 and GT-03 (Figure 4). In addition, data from wells located at < 25 km from the site are available for comparison (W1 till W5 on Figure 1a). The data indicates the presence of 3 main interfaces related to four main geological units namely unconsolidated Cenozoic sediments, the Cretaceous chinks, Upper Carboniferous siliciclastic rocks and the Lower Carboniferous carbonate rocks (Figure 4a-b). The interfaces are clearly visible from abrupt increases in the P wave velocity. The most significant increase is visible at 600 m, marking the transition from the Cenozoic sediments to the Cretaceous chinks, and around 3 km depth, marking the transition from the Upper Carboniferous siliciclastic deposits to the Lower Carboniferous carbonate rocks.

A striking observation in terms from well GT-01 is the presence of a very high ratio $V_p/V_s > 3$, with shear wave velocity V_s being around 500-600 m/s and compressional wave velocity V_p close to 2000 m/s in the uppermost 600 m (Figure 4b). Such high values are generally for unconsolidated sediments in the near surface but rarely observed at several hundred meters depth. The high ratio could be confirmed by analysing the arrival times of multiple P and S wave reflection phases between the free surface and the strong velocity contrast at 600 m clearly visible in the seismograms (Figure 4 and Appendix B). Especially for borehole sensors at around 300 m depth (MOL2A and MOL4), multiple P wave and two distinct S wave phases are visible (Appendix B). Relative arrival times of these phases are in very good agreement with the theoretical arrival when assuming steep reflection angles and almost vertical ray paths between the free surface and the 600 m interface, and velocity values indicated by the well logs (Figure 4b). Furthermore, several forward modelling tests have been performed using

AXITRA code (Coutant, 1990; Cotton and Coutant, 1997) to produce synthetic seismograms which consistently reproduce the observed multiple reflection phases.

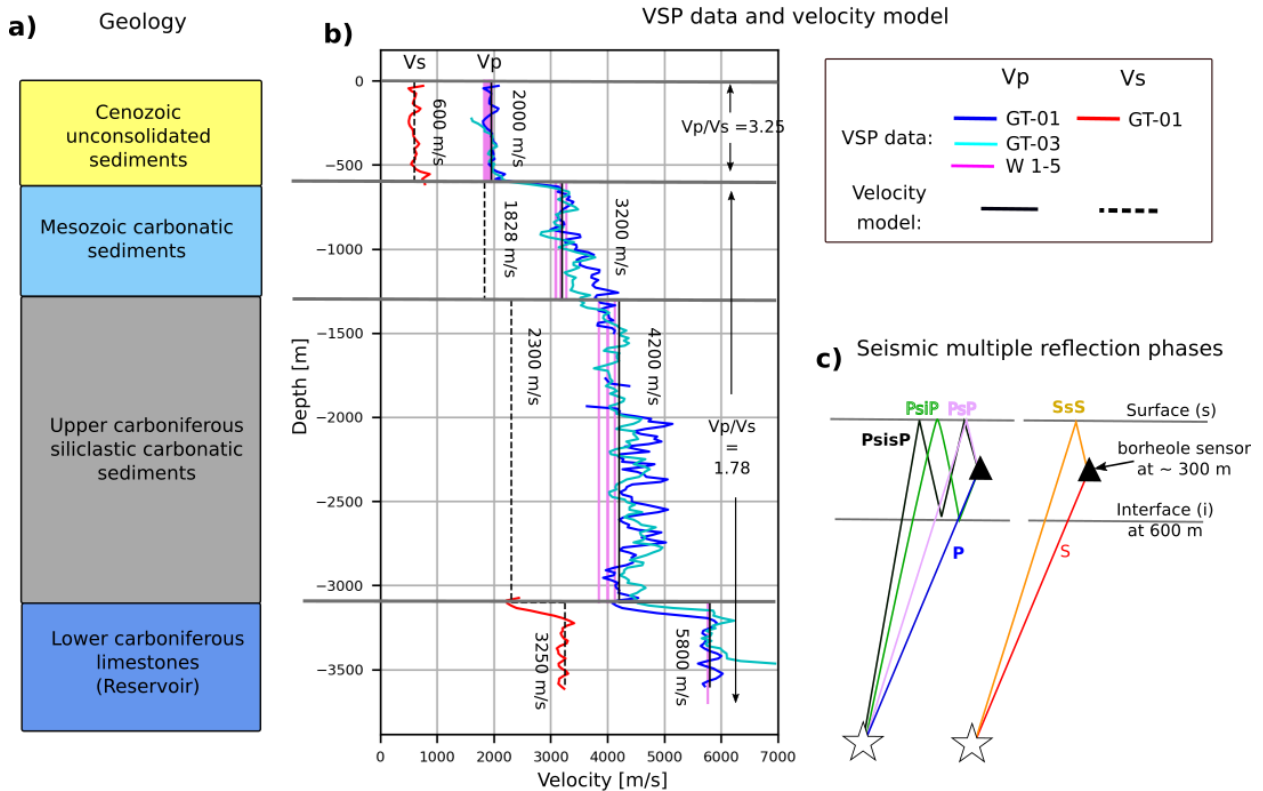


Figure 4: Velocity model: (a) stratigraphy adapted from Bos and Laenen (2017). (b) well log data from GT-01 and GT-03 and other Vp VSP data sets from boreholes W1-5 (pink lines) whose locations are shown in Figure 1b, and the final velocity model used in this study (black lines). c) schematic illustration of multiple P and S wave reflection phases between the surface (s) and the 600 m interface (i) which are all visible in seismograms from ~300 m borehole stations (Figure B1a).

3.2 Source locations

Based on the constraints from well-logging data and seismogram phase interpretation (Section 3.1), we constructed a 1D 4-layered velocity model used for event localization (Figure 4b). Events are located using P and S wave arrival time picks and a probabilistic location approach

accounting for picking errors using the approach by Contrucci et al. (2010) (Appendix B). Picking was done based on filtered seismogram traces at 10-50 Hz (to reduce stronger electronic noises at 1-10 Hz). Picking and location showed that only 51% of the total 267 catalogued events could be located with certainty, which included events with $M_L > 0$. This low location performance is mainly related to the comparatively low detection capacity of the closest station DSLNZ (see also Section 2.3). Locating without station DSLNZ and with at least 3 other stations (ex: DSLB, MOLT and MOL2A) allows to increase the location capacity up to 80% of the total detected events. However, we noticed that the ellipsoid in location uncertainty significantly increases for these cases ($> 1\text{km}$) which may lead to wrong interpretation.

Obtained hypocentre locations for the 138 reliably located events are shown in Figure 5. All events seem to be located several hundred meters to the west of the injection well and occur in the form of two main clusters. The absence of seismicity at the close vicinity of the open hole section of the injection well raises questions regarding the absolute location of the events, as the first events are expected to occur close to the injection zone. Several tests have been performed to evaluate the validity of the event location and to exclude potential bias from the used velocity model and/or picking uncertainty which are all described in Appendix B. None of the performed tests and further analyses on complementary data sets showed evidence for such eventual bias nor evidence for the presence of any significant 3D velocity effect that could explain this unexpected event location. We furthermore examined the remaining low magnitude catalogued events (with higher location error) for seismogram signatures (e.g. ts-tp arrival times) that would suggest an event location closer to the injection point. However, all these events showed strong similarities in waveforms to the well-located events (see following Section 3.4 in this respect).

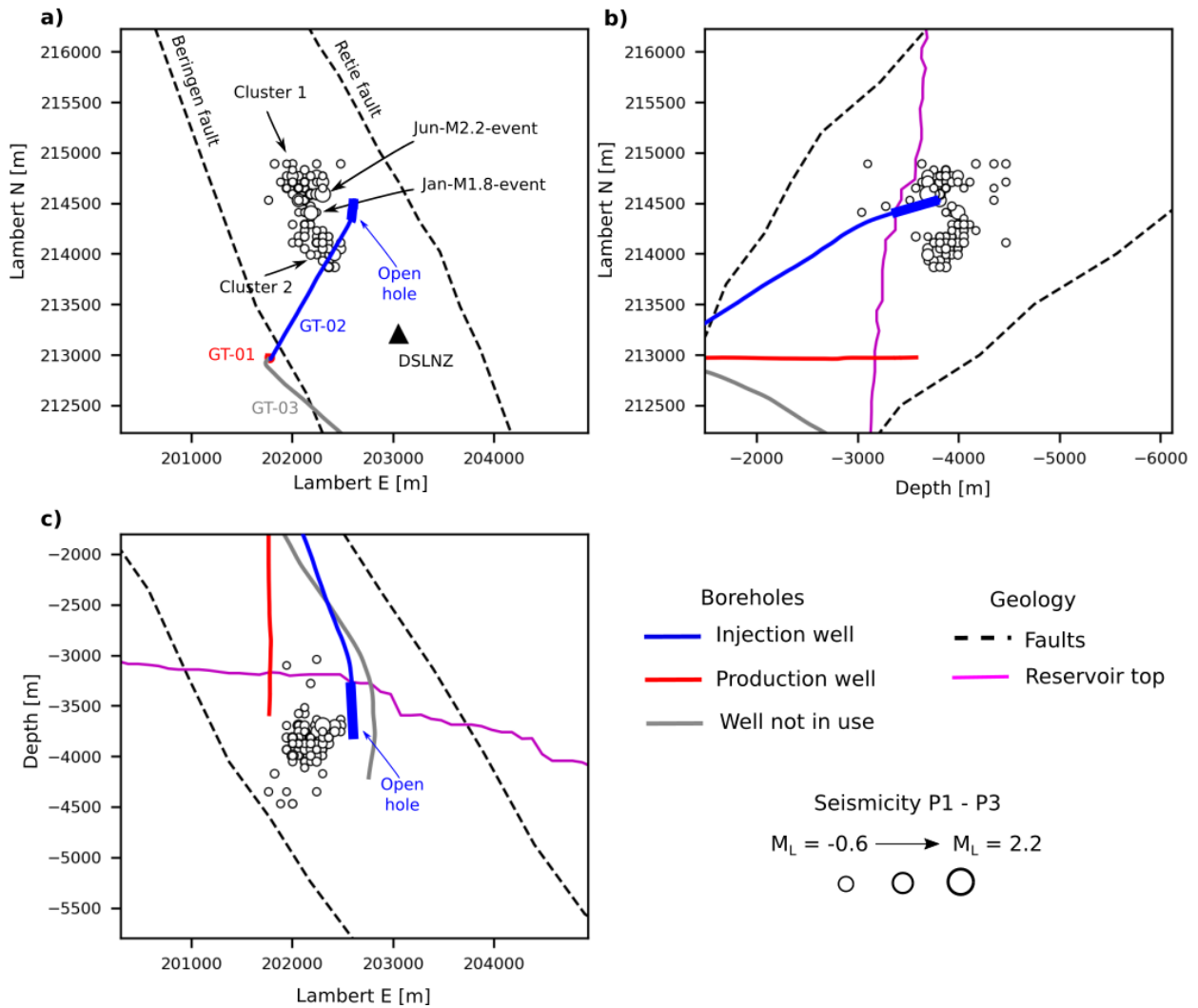


Figure 5: Absolute event locations obtained for 138 events (visible at station DSLNZ and at least 3 stations, see text) using a 1D velocity model (Figure 4b). Note thick blue line marks the open section of the injection well GT-02.

3.3 Multiplet analysis and relocation

As visible from Figure 2 and Figure 5, seismic events tend to occur in temporal and spatial clusters. To characterize the clustering behaviour in more detail we examined the similarity between waveforms of event pairs to identify potential families of multiplets which may provide information on fault patterns and characteristics. For this respect, we applied the equivalence class method by Shanks (1993) based on a high correlation coefficient (> 0.8) criterion,

meaning that event pairs associated with a correlation coefficient greater than this threshold were grouped in the same family. The details of the clustering approach are documented in Appendix C1. The threshold was considered to be the best compromise in order to provide a maximum number of detected multiplet events and families (Appendix C1) and guaranteeing a good visual waveform similarity (Figure 6). With the threshold, we find that more than 60 % of the recorded events are doublet or multiple events which could be grouped into seven and eight families, respectively (Appendix C1). Each multiplet family is composed of several to several tens of events showing high similarity in body wave phases and coda (Figure 6). The multiplet families are clearly distinguishable from each other and differ in absolute location (Figure 7c), confirming the reliability of the clustering approach.

Temporal activity of each multiplet family is shown in Figure 7a-b. Family names have been chosen chronologically relative to the occurrence of the first multiplet event of each family. It is observed that multiplet families 1 - 4 occurred in almost all circulation test phases P1-P3. With a total of 37 events, family 1 seems to be the most recurrent multiplet. It also includes most of the strongest events as the Jan-M1.8-event and Jun-M2.2-event. Family 2 and 3 represent the second and fourth largest multiplet groups with 32 and 22 events, respectively, meanwhile magnitudes of the events are comparatively low with M_w mostly < 0.6 . Families 5 - 8 are widely initiated in P3.4. Stronger $M_w > 1$ events are observed in family 5 and 6 while family 5 represents the third largest family with a total of 24 multiplet events.

A relative location approach (relocation) like the one used by Kinscher et al. (2020) was applied for the events of each multiplet family using all network stations as documented in Appendix C2. For most families the relocated events seem to highlight (sub)vertical lineaments, but often event numbers are too low to observe any clear trends (Figure 7c). For some families (1, 6 and 8), events show partially East-West lineation trends which however need to be considered with caution since bias from the limited station number and azimuthal coverage to the results cannot be completely excluded here (Appendix C2).

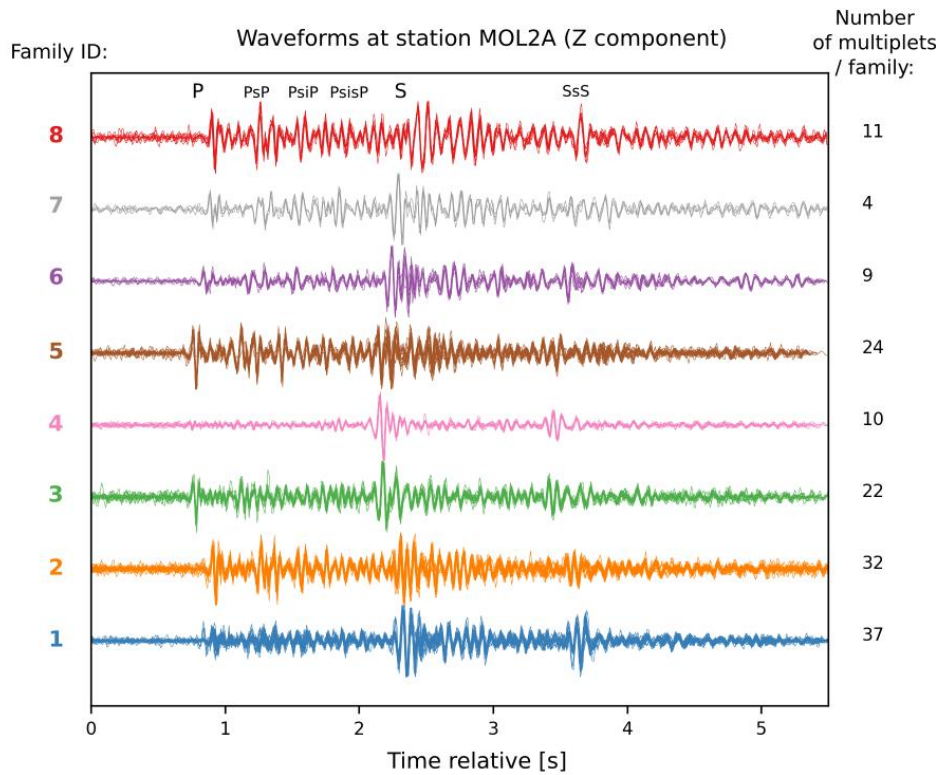


Figure 6: Waveforms of eight multiplet families. Normalized waveforms for each family are aligned by means of the delay times estimated from cross-correlation. Number of events plotted for each family are shown by black numbers on the right side. Family ID are shown on the left.

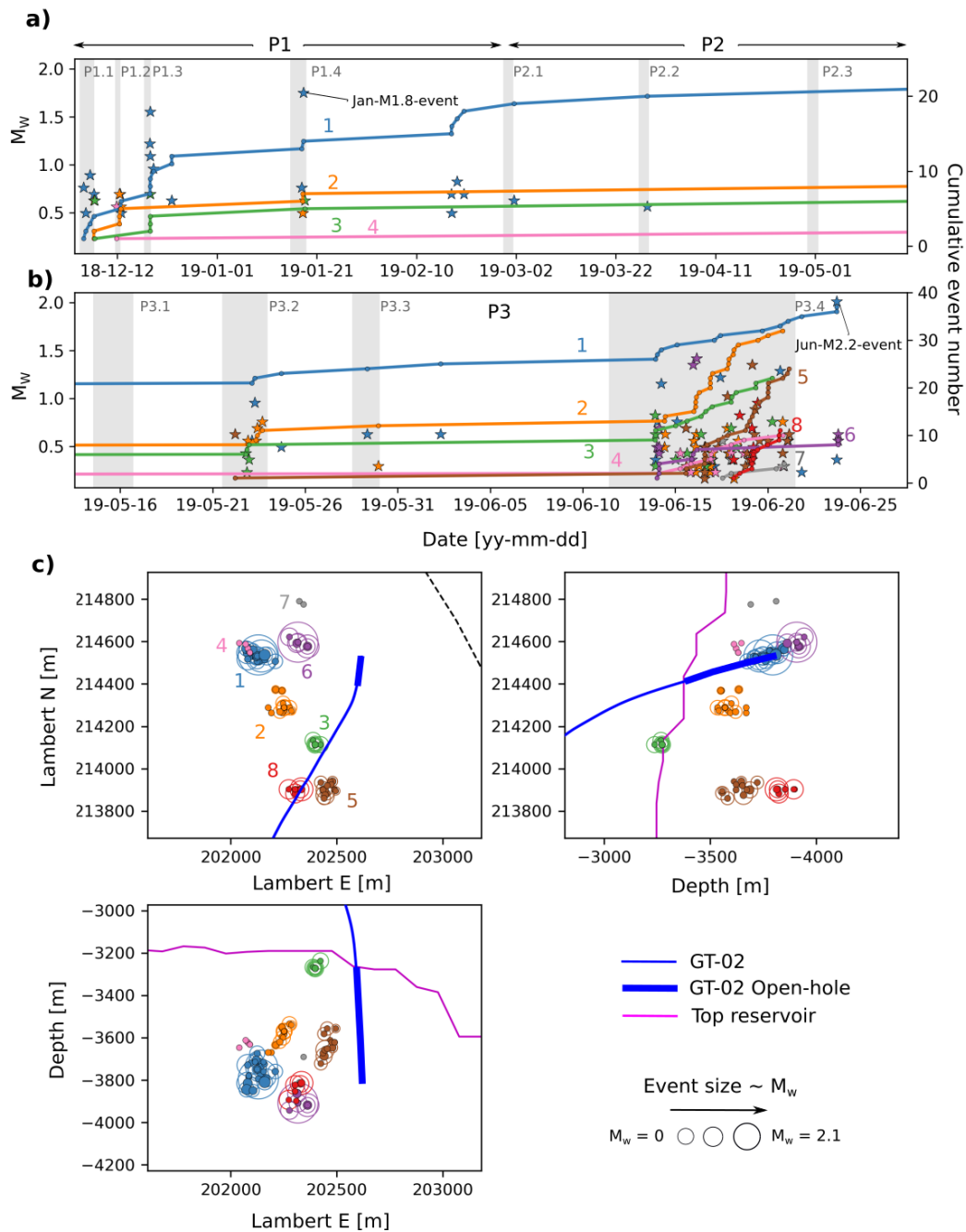


Figure 7 Temporal and spatial distribution of multiplets of families 1-8. a)-b) Cumulative number (coloured lines) and moment magnitude (coloured stars) of multiplet occurrences for injection tests P1-P3 (Figure 2); For M_w estimation please see caption of Figure 3; c) relative locations for multiplets of each family and source radii (circles) estimated from source spectrum analysis as presented in Appendix D. In blue is shown the trajectory of the GT-02 well. In pink, the top of the Carboniferous Limestones

3.4 Multiplet-repeater classification

The high similarity in wave forms observed for certain multiplet families (e.g., Figure 6) may point to the presence of seismic repeaters, i.e., seismic events originating from “exactly” the same location and sharing the same source mechanism. Seismic repeaters are generally interpreted as the repeating rupture of an asperity on a creeping fault (Figure 8a) and thus, are mostly indirect evidence for the presence of aseismic motions. Alternative mechanisms behind repeater occurrence may involve a sequence of successive partial stress release or localized pore pressure increases along specific fault patches (e.g. Duverger et al., 2018). Distinction between seismic repeaters and multiplets, i.e., similar seismic events originating from neighbouring fault segments and/or asperities, is not straightforward and is the subject of current research (e.g. Uchida and Burgmann, 2019).

Here, we follow the concept by Bourouis and Bernard (2007), Cauchie et al. (2020) and Kinscher et al. (2020) and estimate qualitative source overlap for multiplet families. From this approach it is suggested that seismic events can be classified as seismic repeaters when the source radii of the individual events are significantly larger than the interspacing between them (Figure 8b). In contrast, when source overlap is small, events are interpreted as multiplets which represent a rupture process involving several interacting or coupled neighbouring faults and/or asperities. Source radii were derived from the corner frequency of the source spectra using a limited number of stations and frequency band. They have to be considered as a first order approximation only (Appendix D). Furthermore, source radii estimation is highly model dependent and influence the classification results significantly. Here we used the Madariaga model (Madariaga, 1976) which provides the smallest source radii compared to most common models and thus represents a comparatively strict criterion for repeater identification.

Relative event locations are shown together with source radii in Figure 7c. From this illustration (and ignoring uncertainties in source radii and relocation) we suggest the presence of seismic repeaters seems likely in some cases (e.g. family 3 and 8) highlighting the potential presence of aseismic creep (see discussion in Section 5.3). In most cases however, the families seem rather to represent repeater-multiplet transitional cases and thus seem to be related to both, repeat ruptures of asperities potentially loaded by surrounding creep as well as progressive rupture dynamics on the same or neighbouring asperities of the same fault plane and/or on neighbouring fault segments (i.e. successive partial stress release and/or stress transfer).

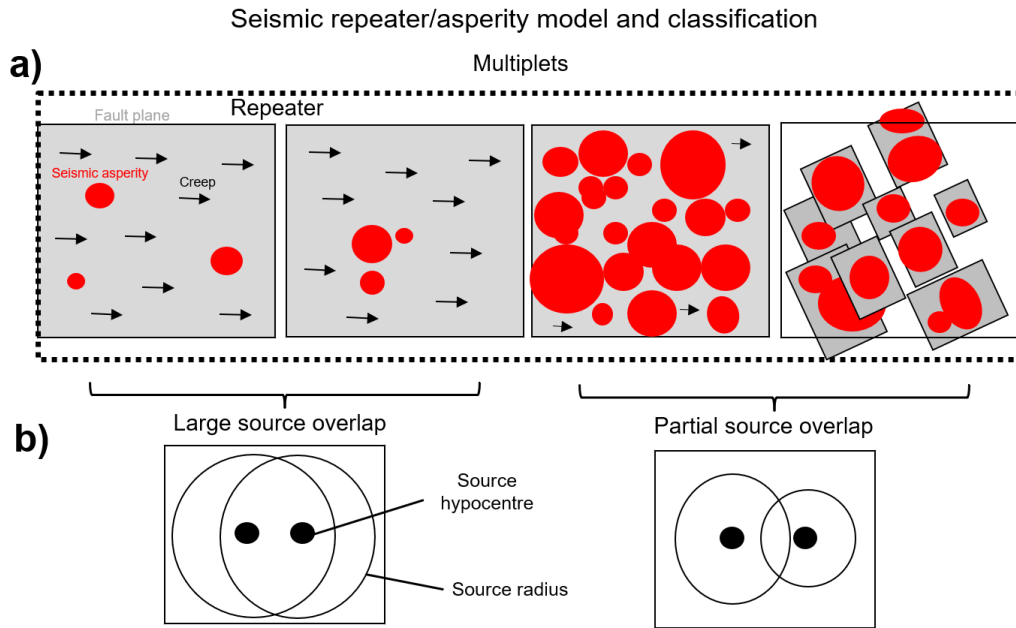


Figure 8: Conceptual model and classification of repeaters and multiplets adapted and modified from Bourouis and Bernard (2007) and Kinscher et al. (2020).

3.5 Source mechanisms

Source mechanisms were analysed for the strongest events in the catalogue, namely the ten $M_L > 1.0$ seismic events (Section 2) based on the wave form inversion approach explained in Appendix E1. The main reason for the limited event selection was to assure a high signal to noise ratio at station DSLNZ which was considered crucial to guarantee good quality results mainly in terms of source sphere coverage (especially incidental). Wave form similarity analysis based on cross-correlation and visual inspection at station DSLNZ allowed to subordinate the ten events into five groups named MECA 1 –to MECA 5, each supposed to have a common source mechanism (Table 1). High waveform similarity ($C > 0.9$ at all stations) observed for events of MECA 1, 2 and 5 allowed us then to improve the signal to noise ratio by waveform stacking. MECA 3 and 4 are composed by only one event. Note that events included in MECA 1, 2 and 3 actually belong to multiplet family 1 as initially classified from station MOL2A (Table 1, Section 3.3) and thus represent sub-families as explained in previous Section 3.4.

Source mechanisms obtained for MECA 1 - 5 are shown in Figure 9. Solutions are all very similar and indicate predominant overall strike-slip faulting either striking NNE-SSW or WNW-ESE (Figure 9a). Results have been evaluated in terms of robustness by means of several sensitivity tests (Appendix E). They are consistent with P wave polarities (Figure 9a) and usually show a very good agreement between synthetic and observed seismograms (Appendix E2). NNE-SSW and W-E to WNW-ESE orientation are very similar to the fault orientation in the reservoir as deduced from borehole observations and imaging data at GT-01 (Figure 9b). Azimuths of the pressure axes of the source mechanisms seem also widely compatible with the orientation of the maximum horizontal stress (S_H) of \sim N330°-N350°, even though a slightly better agreement is observed for MECA 3-5 (Table 1).

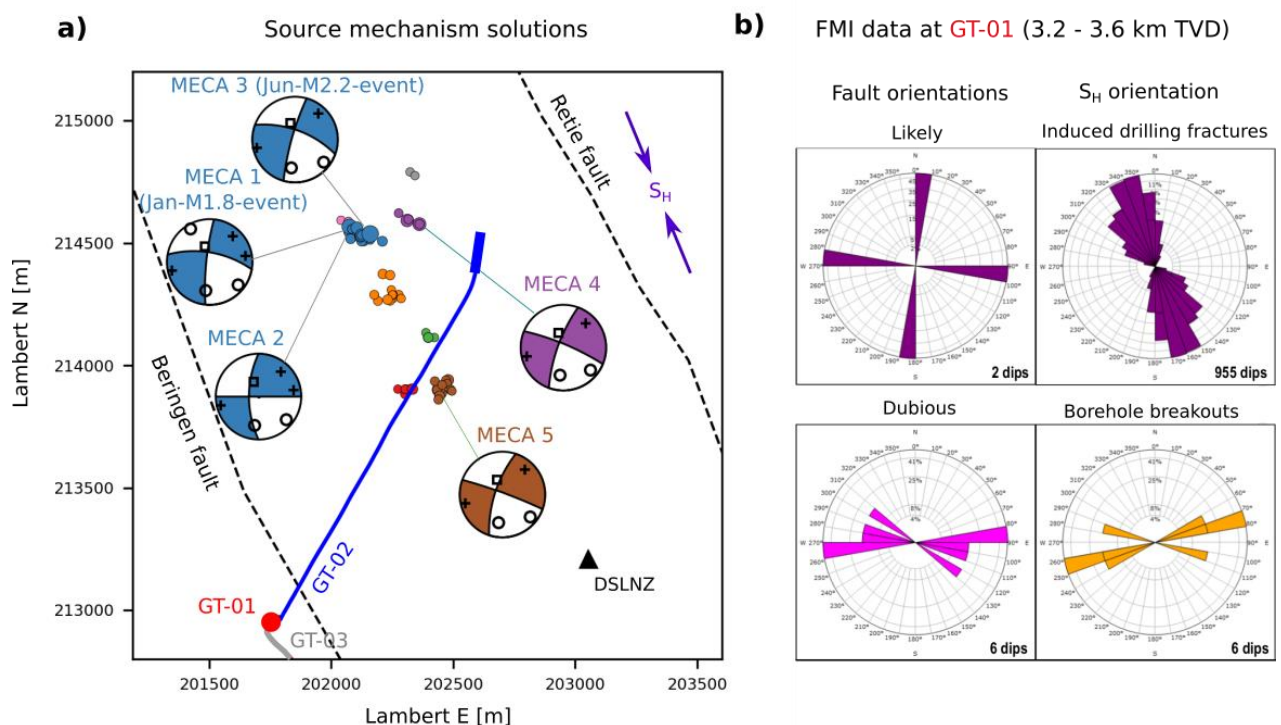


Figure 9: Results of source mechanism inversion. a) lower source hemisphere projection of obtained source mechanisms (beachballs; white= dilative, colour = compressive) for the five event groups MECA1-5 of Table 1. Positive (black cross) and negative (black circle) P wave polarities of all available stations (see Appendix E2) are projected into the beachball sphere. b) results from Fullbore Formation Micro Imager (FMI) in borehole of GT-01 between 3.2 and 3.6 km depth; Likely and dubious fault orientations are defined as clear and less clear

evidence of separation and displacement of layering or structural dip change with a change in open hole log responses; stress orientation is deduced from induced drilling fractures (direct indicators of maximum in-situ horizontal stress direction) and borehole breakouts (symmetrical near-parallel features appearing as a pair of obscured stripes related to shear failures of the borehole wall caused by the present day in-situ stress).

Table 1: Source mechanism analysis of five highly similar event groups (MECA 1-5). Nodal plane orientations and sense of faulting expressed in strike (*str*), dip and rake (*rak*) and related Pressure axis azimuth and plunge for the obtained source mechanisms and related misfits (L2-norm) calculated from synthetic and observed wave forms for all stations (Appendix E).

Group name	ID Multiplet family	Event Date and Time [YYYY-MM-DD HH :MM :SS]	M_L	Str 1	Dip 1	Rak 1	Str 2	Dip 2	Rak 2	Azimuth P-axis	Plunge P-axis	Min. Misift	# of available stations
MECA 1	1	2018-12-18 14:05:19	1,5	280	65	-170	185	80	-25	N°140	65	0.31	6
	1	Jan-M1.8-event	1,8										
MECA 2	1	2018-12-18 12:39:57	1,0	270	90	-155	180	65	0	N°132	72	0.32	5
	1	2019-06-14 05:37:14	0,9										
	1	2019-06-17 10:17:06	1,0										
	1	2019-06-20 15:46:25	1,1										
MECA 3	1	Jun-M2.2-event	2,2	290	65	-170	195	80	-25	N°150	65	0.28	5
MECA 4	5	2019-06-19 03:48:43	1,2	290	85	-160	200	70	-5	N°152	72	0.29	5
MECA 5	6	2019-06-15 23:11:37	1,2	290	80	-165	200	75	-10	N°153	72	0.28	5
	6	2019-06-16 03:27:04	1,8										

4 Reservoir characteristics

4.1 Revision of the structural reservoir model

The geological structure of the Balmatt site (e.g. Broothaers et al., 2021) could be widely confirmed as particularly for the shallower parts at < 600 m by detailed wave form analysis (Section 3.1). Even though this zone is not directly part of the target reservoir itself, it is worth here to underline the anomalous high V_p/V_s ratios (> 3) associated with this rock formation, namely the unconsolidated Cenozoic sediments. Regarding its important thickness at Balmatt and other potential adjacent geothermal sites, we emphasize the importance to account for

these unusual seismic wave propagation characteristics in the velocity model used for seismic monitoring in order to avoid biased source locations and potential misinterpretation in terms of reservoir characterisation and seismic hazard.

The seismic cloud has a clear elongated shape, oriented NNW-SSE, which is in agreement with the direction of the maximum horizontal stress S_H (Figure 9b and Figure 10). As shown from source mechanisms analysis and borehole data, the larger seismic sources are dominated by strike-slip faulting oriented WNW-ESE and/or NNE-SSW. Taken both observations together we propose a new conceptual model as shown in Figure 10c. Our observations support the existence of an unknown pre-existing fracture zone oriented N165E, parallel to S_H , with a dip of $\sim 70^\circ W$, which involves a system of conjugated faults, comparable to an en-échelon type shear zone as proposed at other geothermal sites (e.g. Häring et al., 2008).

The orientation of the suggested NNW-SSE trending and westwards dipping fracture zone seems generally in agreement with some secondary fault segments as known from active seismic experiments (Broothaers et al., 2021). However, these structures could be only observed down to depth of around 2 km whereas fault orientation at the reservoir depth remained widely unknown. Unfortunately, relocation results and related uncertainties do not allow to unambiguously deduce more detailed fault model including shear sense with respect to the activated conjugated structures. Assuming an en-échelon faulting type would probably imply a dominance of NNE-SSW strike-slip faults which seems also more likely from a geomechanical point of view (see later Section 5.1).

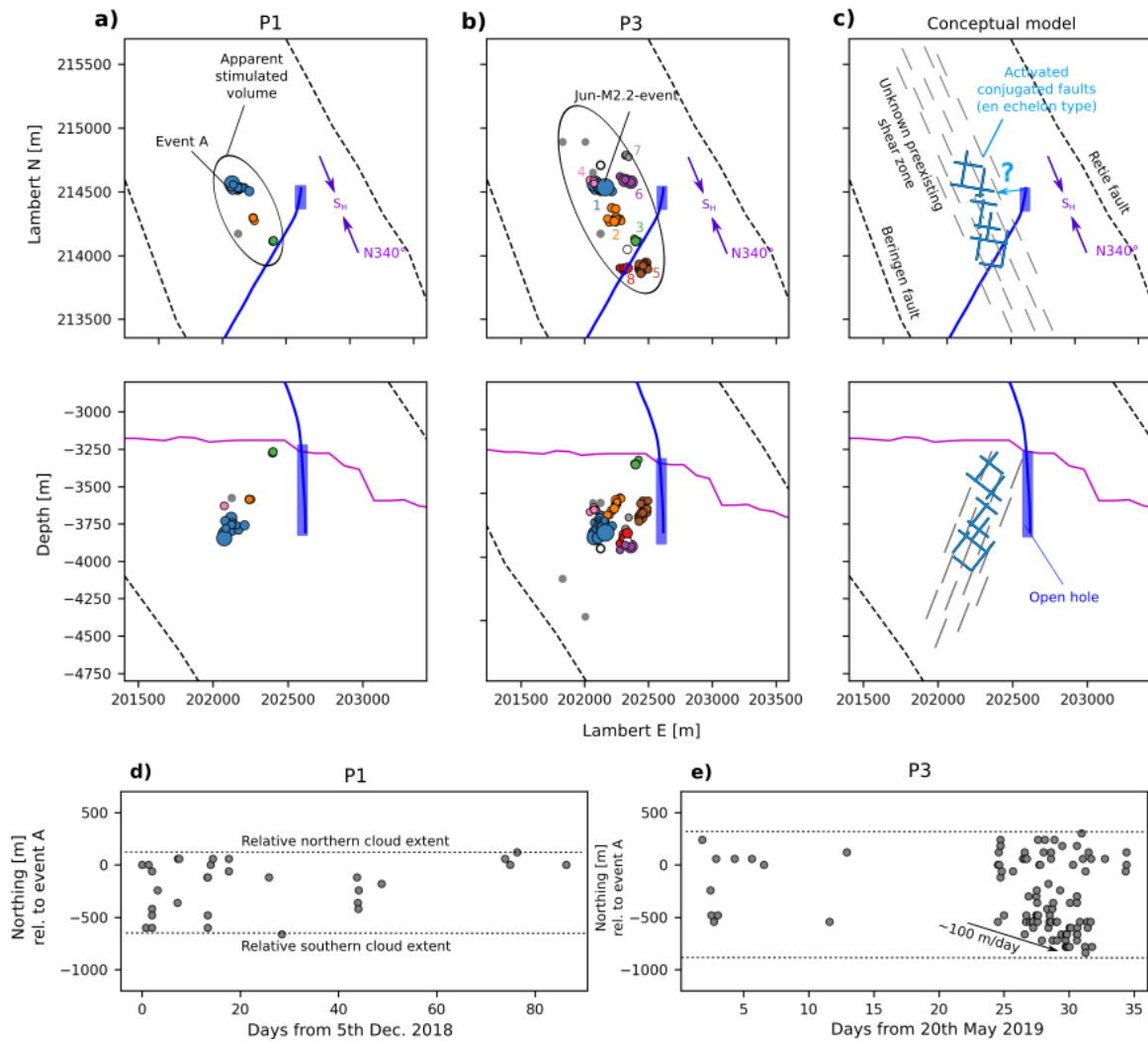


Figure 10: Elongation and growth of the seismic cloud. a)-b) Absolute location of singlets (grey points) and doublets (white circles) and relocation of multiplet families (coloured circles) for injection phases P1 and P3, respectively, in top view (upper panels) and side view (lower panels); see Figure 7 for colour code of multiplet families. c) conceptual model as similar to Håring et al. (2008) showing a potential high permeable pre-existing fracture zone oriented parallel to S_H (grey dashed area), involving conjugated faults oriented NNW-SSE and WNW-ESE (blue lines) which seems to be hydraulically connected (question mark) to the open hole injection well section, eventually by the intersection by the fracture zone or by the hydraulic opening of fractures during previous stimulation jobs (see text). d-e) Northing and Southing relative to the first well-located event (event A in a)) for injection phases P1 and P3.

4.2 Constraints on hydraulic reservoir characteristics

Our revised conceptual reservoir model involves the presence of a fracture zone. This zone may be considered as a (or the most) permeable and unstable domain in the reservoir around MOL-GT-02 as highlighted by the spatial occurrence of seismicity.

We could hypothesize that this zone extends further upwards and eastwards (when extrapolated), possibly intersecting the upper levels of the open-hole section of the injection well, close to the top of the reservoir at around 3250 m depth (Figure 10). Spinner log run tests in MOL-GT-02 indicated primary losses in the upper and middle part of the open hole section, which would be consistent with the expected intersection area between MOL-GT-02 and the fracture zone (Figure 10). However, no clear evidence could be found that confirmed the presence of a main fracture zone, as no borehole imaging data are available.

From this model we expect the presence of an efficient hydraulic (permeable) connection between open hole section and the “distant” seismic zone. Indeed, efficient fluid pressure diffusion and equalization could be observed from the occurrence of co-seismic well-head pressure increases following two closer and stronger $M > 1.0$ events of family 6 (~ 0.2 - 0.3 bar) and mainly to the Jun-M2.2-event (~ 2 bar) (Figure 11d). An efficient hydraulic connection to the upper part of the open-hole section would also be in agreement with the absence of seismicity around the bottom of the open-hole section (if not simply a result of the limited network detection capacity of $M_c > 0.6$; Section 2.3) where pressure build-up is possibly significantly reduced.

The lack of seismicity in the direct vicinity of the open hole section might also result from newly formed structures with higher permeability, closer to the open-hole section, counteracting a pore pressure build-up. The increased permeability might have been formed due to fracture opening or perhaps even hydraulic fracturing during previous stimulation jobs and injection tests performed in August - September 2016. Indications for initial fracture opening during the 2016 stimulation and testing phase comes from template matching analysis as described in Appendix A. The analysis highlighted a particular group of seismic events recorded during the first 10 hours of the injection phase which never seem to reoccur and whose location might have been closer to the injection well.

As a second hypothesis, we suggest that the fluid diffusion process after injection seems widely characterized by a fracture-dominated fluid flow parallel to S_H . The stimulated volume, i.e. the volume affected by the injected fluid, is thus preferentially oriented in the same direction (Figure 10). Consistently, we observe a growth of the seismic cloud in S_H direction when comparing the difference in cloud size between P1 and P3, which involves the onset of the northern and southern most multiplet families 5, 7 and 8 during P3.4 (Figure 10a-b and *Figure 11b*). For the same period, we also observe a southward spatio-temporal migration trend of the epicentre locations which can be characterized by an apparent velocity (depth of events not taken into account) in the order of 100 m/day (Figure 10e). Even though highly speculative, this approximative linear evolution of the cloud size with time may suggest that permeability in the fracture zone is in a first order homogeneous.

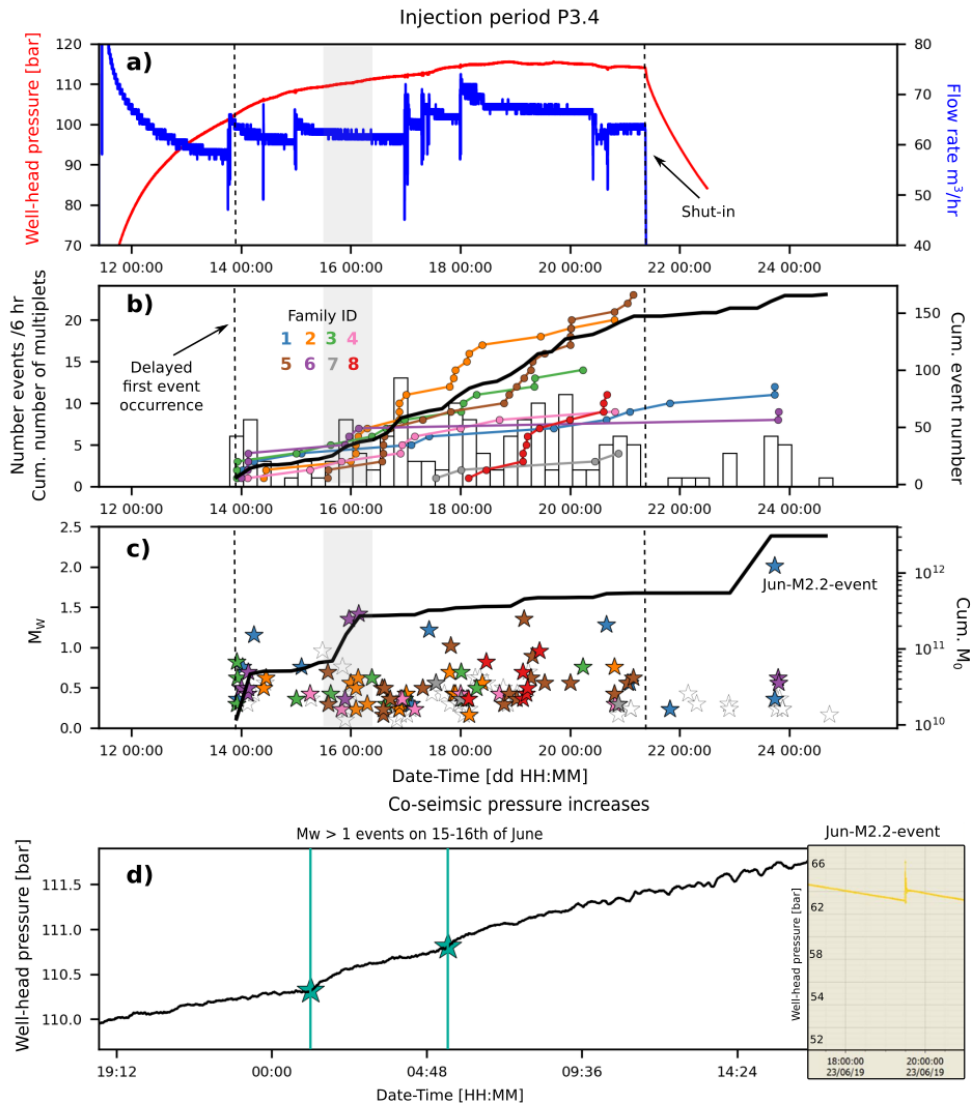


Figure 11 Zoom to injection phase P3.4 in June 2019. a) continuous data (1s sampling) of well-head pressure (black curve) and flow rate (grey curve) measured at GT-02. b) number of detected events (white bars) and cumulative event number curves of multiplet families. c) Moment magnitudes M_w of recorded singlets and doublets (white stars) and multiplet families (coloured stars); see Figure 7 for colour code of multiplet families. M_w were derived from local magnitudes by using the empirical relationship $M_w = 0.66 M_L + 0.56$ (Kinscher, 2020b). This relationship was calibrated based on > 50 events with known seismic moments estimated from their source spectra as described in Appendix D. d) Co-seismic pressure increases for two $M_w > 1$ (zoom to grey shaded area in a)-c)) on 15-16th of June 2019 and during the Jun-M2.2-event (orange curve in right panel) (see text).

5 Constraints on the geomechanic model

5.1 Mohr Coulomb failure criterion

Induced microseismicity in geothermal sites is commonly explained by the reduction of effective normal stress acting on fractures and faults in the subsurface because of pore pressure increase following fluid injection. To test this model, we discuss briefly the Mohr-coulomb failure criterium based on a conservative approximation of the reservoir stress configuration suggested at Balmatt at 3.8 km depth which represents the average depth for seismic hypocenters (Figure 12).

Natural hydrostatic pressure at 3.8 km depth is estimated at 39.2 MPa from direct measurements at the three wells. Vertical stress was integrated from density well logs (e.g. Zoback et al., 2003) and approximated with $S_V = 91$ MPa (~ 51.8 MPa when corrected for hydrostatic pressure; Figure 12). In addition, formation integrity tests (FIT) have been performed providing a lower bound for σ_3 (e.g. Konstantinovskaya et al., 2012). A test at the reservoir top at GT-02 and a gradient derived from other tests at different depths suggests $\sigma_{3min} \sim 54$ MPa (~ 14.8 MPa when corrected for hydrostatic pressure; Figure 12) (pers. comm. VITO). Furthermore, we consider $S_H \sim S_V$ which is actually a strong assumption since the ratio S_V / S_H can significantly vary depending on the tectonic and rheologic setting and can be in particular in sedimentary environments significantly below 1 (e.g. Zang et al., 2012) what implies significant change in the here modelled differential stresses. Obtained source mechanisms indicate a strike slip faulting regime which suggest that $S_H \geq S_V$ and implies higher differential stresses as resulting our $S_H \sim S_V$ assumption. As a second strong assumption, we consider here a no cohesion failure envelope (0 MPa) which approximates the case of a pre-existing fault with very weak frictional behaviour. Finally, we assume that no significant pressure loss occurs between the injection area and the adjacent seismogenic zone which is in agreement with the above discussed presence of a permeable fracture connection zone (Section 4.2).

Mohr circles in Figure 12 show the state of stress for the fault planes deduced from source mechanisms when approximating the maximum pore pressure increase as the sum of hydrostatic pressure and maximum wellhead pressure (under the assumption of zero overpressure and no downhole pressure loss). Considering a wellhead pressure of 7 MPa, as

recorded during the first seismic event occurrences in P1.1 and P3.1 (see e.g. Figure 13), fault failure of the corresponding seismic events, represented by MECA 1-3, is reached for $\mu \leq 0.85$, which is a typical value often assumed for pre-existing faults in low normal stress regimes (< 200 MPa) (e.g. Byerlee, 1978). Assuming similar failure conditions (i.e. $\mu \sim 0.85$), failure for MECA 4-5 is only observed when considering maximum wellhead pressure of 11 MPa, as it was maintained over several days during P3.4 (Figure 11). Accordingly, multiplets related to MECA 4-5 (i.e. families 5 and 6; Table 1) are only observed in P3.4 and in none of the preceding short duration injection phases where such maximum pressure levels were only reached punctually.

Ignoring the strong assumptions on friction coefficients, cohesion, differential stress and pressure loss within and distant from the injection well, these results are in agreement with our conceptual model promoting failure along pre-existing faults with most preferable orientation with respect to S_H . As also discussed in the context of the conceptual fault model (Section 4.1), NNE-SSW oriented fault planes seem to be generally closer to failure condition than the WNW-ESE planes deduced from source mechanisms, when assuming $S_H \sim 340^\circ$ (Figure 12). On the other hand, borehole breakouts show variation of S_H of $330^\circ - 350^\circ$ and faults identified from borehole imaging data show both fault orientations (Figure 9b). The good agreement between the azimuth of the P axes of MECA 3-5 with S_H (Table 1) might alternatively indicate the presence of a conjugated fault system whose failure can be explained by the principle of maximum shear stress theory (Tresca) ignoring differences in their friction properties.

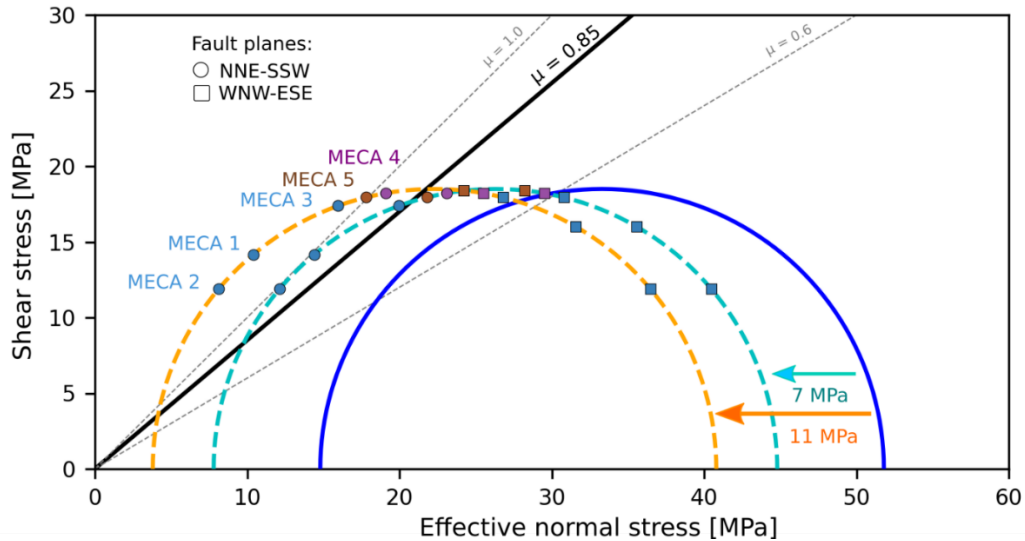


Figure 12 Mohr circles for the initial state of stress approximated by the maximal S_H and minimal S_h compressive effective horizontal stress (deduced from formation integrity tests (FIT) and density logs and accounting for natural hydrostatic pore pressure of 39.2 MPa) at Balmatt (blue circle) at 3.8 km depth and modified state after fluid injection at 7 MPa (cyan circle) and 11 MPa (orange circle), which corresponds to the maximum wellhead pressures reached in P1 and P3 respectively (e.g. Figure 2). Critical shear stress levels are shown for the typical range of friction coefficient $\mu = 0.6 - 1$ considered for pre-existing crustal faults and typically assumed in low normal stress regimes $\mu = 0.85$ (Byerlee, 1978), assuming cohesion to be negligible. Fault planes deduced from source mechanisms MECA 1-5 are drawn on the Mohr circles assuming $S_H \sim 340^\circ$.

5.2 Potential presence of the Kaiser effect

A phenomenon often discussed in the context of pore pressure effects in geothermal environments is the Kaiser effect, i.e. a stress memory effect characterized by the absence of seismicity until the stress level or overpressure of the previous injection experiment is exceeded (e.g. Baisch and Harjes, 2003; Wenzel, 2017; Kluge et al, 2021). Evidence for the Kaiser effect is suggested in Figure 13 where we show the well-head pressure level recorded at the first seismic event detection for the short-term consecutive injection phases in December 2018 (P1) and in May to June 2019 (P3), respectively. For each consecutive injection phase sequence, we observe a constantly increasing pressure level which we interpret as the

signature of a stress memory effect (Kluge et al., 2021). Similarly, the presence of the Kaiser effect may potentially explain the absence of seismicity in P2 and P3.1 (Figure 2b), where maximum pressures remained below the maximum pressure reached during the preceding injection phase P1.4 associated with the occurrence of the Jan-M1.8-event. The Kaiser effect is a potential explanation for the clear temporal delay of seismic activity following injection in P 3.4 (Figure 11) and observed in other injection phases. In this case the first event occurrence is observed at a well-pressure around 100 bar (Figure 11a) which is exactly the maximum well pressure of the preceding injection phase P 3.3 (Figure 2c and Figure 13). Assuming the Kaiser effect is indeed the mechanism causing the observed pressure-level increases would imply that such effects may also play a role in sedimentary reservoirs which seem to haven't been reported so far (e.g., Zang et al., 2014).

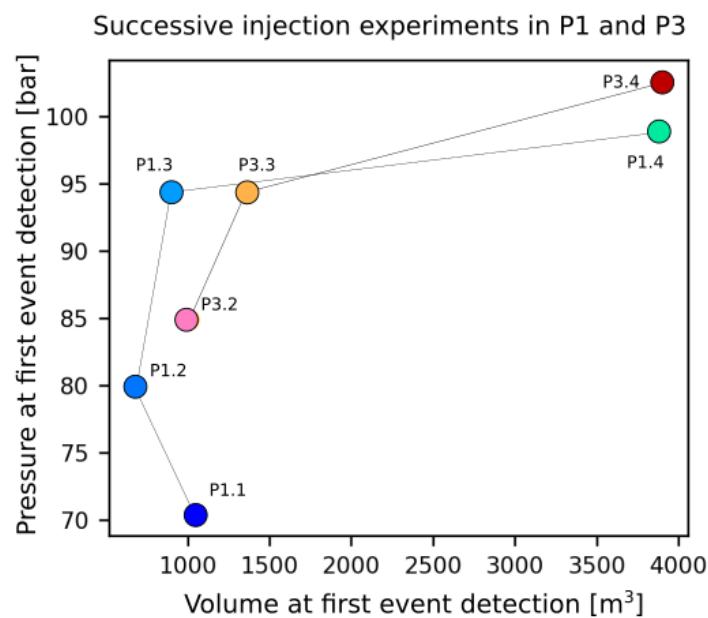


Figure 13 Possible signature of the Kaiser effect; well-head pressure and total injected volume measured at the first seismic event occurrence and their timing relative to the start of injection for successive injections in P1 and P3 (Figure 2; Section 2.2). Colouring is consistent with respect to Figure 14 to allow for better distinction between different injection phases.

5.3 Potential role of aseismic slip

The favourable condition for aseismic movements (stable fault slip) in geothermal environments and its important contribution to triggering of seismicity have been demonstrated from several geothermal injection experiments (e.g., Bourouis and Bernard, 2007; Cauchie et al., 2020; Cornet, 2016; Cornet et al., 1997; Hopp et al., 2019; Lengline et al., 2014, 2017; Wei et al., 2015), small scale injection experiments (e.g. De Barros et al., 2019; Guglielmi et al., 2015; Huang et al., 2019) and hydromechanical modelling (e.g. Jeanne et al., 2015; Wynants-Morel et al., 2020). Since Balmatt reservoir characteristics are widely comparable to these cases (e.g. in terms of relatively shallow depth), aseismic movements are generally expected to occur.

Even though no direct evidence could be provided from the data and our analysis, some evidence is suggested from the potential presence of seismic repeaters (Section 3.4). It remains however questionable here if the repeating nature of seismicity represents a creep triggered repetitive failure of fault patches or an (pore pressure controlled) accelerated loading-rupture cycle or an interplay of very closely located faults. Some further evidence comes from low stress drops as deduced in Appendix D which might (when ignoring important underlying uncertainties) reflect the effect of normal stress reduction on the fault planes from fluid pressure which stabilize slip (e.g., Cauchie et al., 2020; Lengline et al., 2014). Also, strong stress-drop variations are observed for each multiplet family (Appendix D) which may eventually reflect transitions from stable (aseismic dominated; favoured by injection lowered normal stresses due to high pore pressures) to a more unstable slip friction behaviour of the fault (see also Section 6.3). In addition, the location of seismicity relatively distant to the injection area could be potentially seen as a consequence of stress perturbation from aseismic movements (e.g. De Barros et al., 2016; Duboeuf et al., 2017; Guglielmi et al., 2015; Wei et al., 2015). Finally, larger aseismic slip and resulting stress perturbations could also represent one of the key mechanisms explaining the late post-injection seismic activity (e.g., following P1.4, Figure 2) which seems less compatible with a continuation of the fluid diffusion process (e.g. Baisch et al., 2010).

6 Seismic hazard

6.1 Implications from the revised structural reservoir model

The generation of higher magnitude events ($M > 4$) requires the presence of longer rupture zones (> 500 m) such as the main regional faults, namely the Retie and Beringen fault. However, from seismic source locations, we conclude that both faults are probably not involved in the generation of seismicity and thus appear rather hydraulically isolated from the injection area. Following our conceptual fault model from Section 4.1, we suggest the presence of an immature fracture zone composed of conjugated small-scaled faults. The generation of large dynamic rupture events seems thus less likely. Nonetheless, the generation of stronger $M > 3$ events appear not out of the question and has been also observed during the stimulation of similar fault settings as the Basel case (Håring et al., 2008) and the recent Strasbourg case (Schmittbuhl et al 2021), even though reservoir depth and geology and not directly comparable here.

6.2 Relation between injected volume and M_{Max}

Seismic hazard assessment in geothermal injection experiments is mostly discussed in the context of the expected maximum magnitude M_{Max} whose estimation has been attempted in various ways using seismic and production data (e.g., Baujard et al., 2014; Hallo et al., 2014; Gaucher et al., 2015; Kwiatek et al., 2015; Orlecka-Sikora and Cielesta, 2020; Shapiro et al., 2011; Zang et al., 2014). Here we limit our discussion to the most popular physical-based models by McGarr (2014), Galis et al. (2017) and the probabilistic model by Van der Elst et al. (2016) (hereafter called the *McGarr*, *Galis* and *Van der Elst* models) which aim at explaining the upper limit of an apparent empirical scaling relationship between the total injected volume and the maximum observed magnitude found from a global data base of different injection experiments (McGarr, 2014). In addition, we discuss the cumulative seismic moment release with fluid injection to highlight a potentially hazardous evolution by following the recent approach of Kwiatek et al. (2019) and Bentz et al. (2020).

The cumulative evolution of the seismic moment M_0^{cum} as a function of the injected volume through time from the beginning of the stimulation and the total seismic moment M_0 release as a function of the total injected volume, are shown in Figure 14 for the different circulation

phases at Balmatt in comparison with the three prediction models. We notice an apparently proportional increase of the cumulative moment with the injected volume (Figure 14a) whose trend ($M_0^{\text{cum}} \propto (V_i^{\text{cum}})^{3/2}$) seems to be best in agreement with the models by *Galís* and *Van der Elst*. The observed proportionality is generally in agreement with our suggested fracture zone (Figure 10c) and suggests that its interior fluid rock behaviour can be approximated by linear poro-elasticity (i.e. proportional scaling between change in pore pressure and injected volume; homogeneous fluid pressure equalization) (e.g. Shapiro et al., 2007; Wang, 2000) as a possible consequence of constant permeability (Section 4.2). The deviation of the observed $M_0^{\text{cum}} \propto (V_i^{\text{cum}})^{3/2}$ trend to the *McGarr* model can be potentially related to the difference of the model concept, assuming a spherical stimulated volume in contrast to a fracture zone and non-simple volume shape as in our case, which may result in a misestimate of the predicted strain energy. Still, the significant discrepancy in absolute moment release can be theoretically explained by the presence of larger scale aseismic movements (e.g. McGarr and Barbour, 2018). To a certain extent the discrepancy (also partially observed for the *Galís* model) can be related to a complexity of the fault zone geometry and to the fact that eventually a certain volume of fluid is effectively removed from the reservoir as a result of the circulation setting including pumping at GT-01 (depending on its hydraulic connection to the stimulated reservoir which is not fully understood).

Some deviations from the $M_0^{\text{cum}} \propto (V_i^{\text{cum}})^{3/2}$ trend are observed by the comparatively steep increase of the cumulative seismic moment for P1.3 and P1.4, but also for P1.2, P3.3 and the beginning of P3.4. Since seismicity is stable in location and mechanism over all the circulation phases (as indicated by the high percentage of multiplets), we do not believe that these trends indicate a hazardous evolution (e.g. transition to unstable faulting regime). Instead, since all the concerned phases were preceded by a prior injection phase, we rather suspect that these trends are somehow related to the Kaiser effect (Section 0). In this context, we would expect that the steep trends will level up to the $M_0^{\text{cum}} \propto (V_i^{\text{cum}})^{3/2}$ trend when exceeding the total injected volume of the previous injection phase (assuming similar injection rate) as partially visible for P3.2-3.4. Consistently, a clear $M_0^{\text{cum}} \propto (V_i^{\text{cum}})^{3/2}$ is visible when summing up the evolution over all injection phases for P1 and P3 as shown in Figure 14a. Following the same reasoning we may also explain the unusually high seismic moment release for P1.3 (i.e. apparent exceedance of Van der Elst criteria), for which the injected volume was in fact

significantly higher as shown in Figure 14b when considering the remaining volumes of the two closely preceding injection phases P1.1 and P1.2.

Despite the good agreement of the data to the *Galís* and *Van der Elst* models, it remains at this point highly questionable what these apparent qualitative differences in the model-data fit concretely imply regarding the interpretation of the actual physics dictating the size and timing of M_{Max} at Balmatt, which are very different for each of these models. Following *Van der Elst*, the observed good model-data fit may imply that the expected M_{Max} at Balmatt is time independent and depends alone on the sampling statistics of the Gutenberg-Richter magnitude-frequency distribution, i.e. on the governing tectonics (as e.g., geometry, dimension, stress, friction etc.) as is the case for natural earthquakes. In contrast, the non-dynamic fault model by *Galís*, states that M_{Max} is determined by competition of injection induced fluid pressure and tectonic prestress leading to an either self-arrested or runaway rupture, i.e., a spontaneous rupture stop a finite distance to nucleation or a rupture stop controlled by the boundaries of the fault. In the case that the observed M_{Max} at Balmatt is below the suggested law in Figure 14, might imply that rupture is self-arrested meanwhile M_{Max} above would correspond to a runaway rupture (not predictable by the model). The timing of M_{Max} in this model depends directly on the injected volume and thus gets more probable with ongoing injection which is different compared to the *Van der Elst* approach.

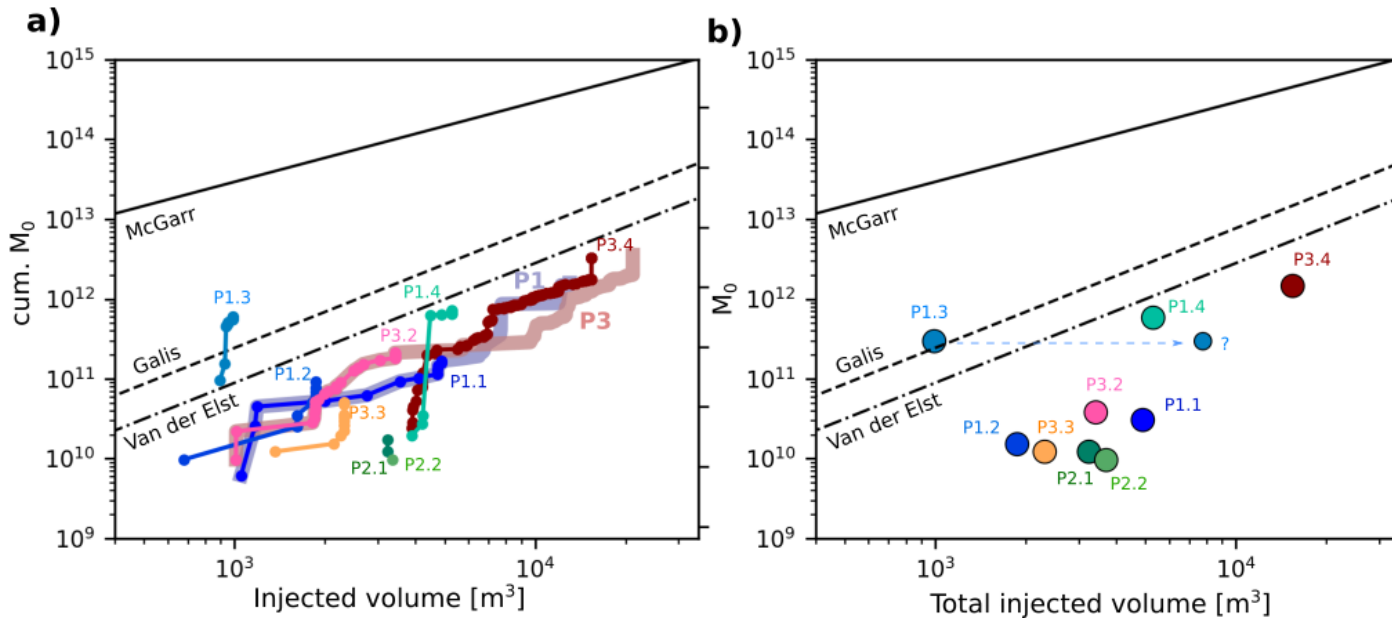


Figure 14 Comparison of seismic moment release and injected volume for each circulation phase (e.g. Figure 2) shown as cumulative evolution a) and by its total amount and maximum moment magnitude, respectively b). Dashed arrow of P1.3 indicates a potential uncertainty in the estimation of the total injected volume due to potential remaining volumes related to preceding injection tests P1.1 and P1.2. Data sets are shown in comparison to different M_{Max} prediction models proposed by McGarr, Galis and Van der Elst (see text). McGarr's model is shown for a shear modulus of $G = \rho V_s^2 \sim 30 \text{ GPa}$ (with $\rho = 2700 \text{ kg/m}^3$ and $V_s 3.3 \text{ km/s}$; Figure 4) and $b = 1$ (Figure 3). Galis model is shown for same G , an average stress drop of 0.5 MPa (Figure), a reservoir thickness of 1 km and a dynamic friction coefficient of 0.1 . Van der Elst model is shown for a b -value $= 1$ (Figure 3) and an assumed seismogenic index of $\Sigma = -1.8$.

6.3 Prediction of the Jun-M2.2-event

The occurrence of the Jun-M2.2-event seem to be generally in agreement with the trend visible from the cumulative moment and injected volume (Fig. 14a) since the evolution during P3.4 is reaching the Van der Elst criterion. This observation underlines the usefulness of the continuous recording and tracing of these parameters in injection experiments as already shown in previous studies (Bentz et al., 2020; Kwiatek et al., 2019). Nonetheless, the explanation and retrospective prediction of the event occurrence in space and time remains

highly speculative from our results. Like large event occurrences at other geothermal sites, the event occurred after shut in. Often these post-shut-in event occurrences are interpreted as a continuation of the diffusion process towards the outer borders of the stimulated volume (e.g. Baisch et al., 2010). This model seems however incompatible with the event location close to the injection well.

Alternatively, we suggest that two main processes were involved in the triggering of the event in space and time: i) an evolution of the local state of stress field due to repeat (a) seismic fault slip and ii) a change in frictional fault stability following the shut-in forced pressure decrease. Its affiliation to multiplet family 1 suggests that the Jun-M2.2-event occurred in an area likely composed by multiple neighbouring faults (Section 3.4) which repetitively slipped since the beginning of the circulation experiments what may have continuously modified the state of stress of the Jun-M2.2-event segment. The pressure drop in this area, following the shut-in of the longest circulation phase (10 days), may then have re-raised the effective normal stress which lead to a transition from stable to a more unstable slip friction behaviour of the fault (see also Section 5.3). Such mechanisms would be generally in agreement with apparent major changes in stress drops observed for multiplet family 1 (Appendix D; Cauchie et al., 2020; Lengline et al., 2014).

7 Conclusion and outlook

In this paper we provide constraints on the structural and hydromechanical characteristics of the fractured Lower Carboniferous limestone reservoir at the Balmatt site and discuss related seismic hazard. The study is based on the induced seismic events following circulation tests in 2018-2019, which were recorded by a relatively poorly performing seismic network despite being based on deep borehole stations, that we characterized with a magnitude of completeness of $M_c \geq 0.6$. Thanks to detailed data analysis and the application of adapted tools, we tried to overcome challenges associated with the resulting low event number (total of ~ 250 events) and the relatively high completeness magnitude. One important part of the analysis and a precondition for reliable seismic data interpretation and local seismic monitoring operations was the detailed revision of the local velocity model which is characterized by anomalously high V_p/V_s ratios (> 3) down to a depth of 600 m. Evaluation of seismic source locations as well as detailed waveform based source analyses then suggested that seismicity

seems to occur along a pre-existing fracture zone oriented parallel to the direction of the maximum horizontal stress S_H ($\sim N^\circ 340$), dominated by conjugated strike-slip faulting oriented NNW-SSE and WNW-ESE.

Even though we cannot clarify from our results if the main fracture zone directly intersects with the open-hole section of the injection well, several observations confirm their efficient hydraulic connection. Failure of faults thus seems to be related to a direct pore pressure effect in the fracture zone, which is consistent with consideration from the Mohr-Coulomb failure criterium despite strong uncertainties underlying the parametrization of the used friction model. We observe a proportional increase of the cumulative seismic moment and the injected volume following $M_0^{cum} \propto (V_i^{cum})^{3/2}$ which suggests the presence of an approximately linear poro-elastic fluid-rock behaviour in the fracture zone (proportional scaling between change in pore pressure and injected volume), linked to homogeneous pressure equalization potentially resulting from similar permeability of the pre-existing structures.

As an important implication for seismic hazard, our observations evidence presumes that no seismicity is generated from the regional main faults (Retie and Beringen fault) which seem more predestined to create larger dynamic rupture zones associated with larger seismic events ($M > 4$). Instead, it seems that stresses are rather released along a faulted zone that includes a collective system of conjugated small-scaled faults. In terms of seismic hazard mitigation, the observed trends between cumulative seismic moment and injected volume underline the interest to use Gutenberg-Richter statistics as a probabilistic forecast model as suggested by the good fit to the *Van der Elst model* and to monitor the budget of induced hydraulic and seismic energy as e.g., suggested by Bentz et al. (2020) and Kwiatek et al. (2019). However, in contrast to the guidelines of these last-named works, observed deviations from the $M_0^{cum} \propto (V_i^{cum})^{3/2}$ trend were here not interpreted as an indicator for hazardous transition from stable to an unstable faulting regime but rather as a result of the repetitive injection and the presence of the Kaiser effect.

We underline the importance of further investigating the nature of aseismic movements at the Balmatt site which could not be fully proved from our results, but which are potentially involved in the generation of very late ($>$ month) post-injection seismic activity and indirectly in the triggering process of the Jun-M2.2-event. The explanation of these features as well as the variability of the trends between seismic moment release and injected volume (as a basis for

the prediction of M_{\max}) likely require a better understanding of the probably highly non-linear, dynamic interplay between seismic and aseismic fault slip (i.e. transient friction behaviour), the anisotropy of the stimulated volume, and the resulting stress transfer which are very sensible and continuously evolving with respect to the applied injection scenario and changing hydraulic reservoir conditions

Acknowledgement

We thank two anonymous reviewers for their fruitful suggestions which helped to significantly improve the paper. We thank VITO for providing the data and DMT for preparation of the seismic data. In particular we like to thank Justin Pogacnik (VITO) for his contribution on stress state estimates from borehole data and Stijn Bos for fruitful discussions. Stations DSLB and MOLT/MOL4 are owned by NIRAS/ONDRAF and managed by the Royal Observatory of Belgium (ROB). Data from these stations are available as part of a data-sharing agreement. For many processing and imaging steps ObsPy tools (Beyreuther et al., 2010) were used.

References

- Abercrombie, R.E., 2015. Investigating uncertainties in empirical Green's function analysis of earthquake source parameters, *J. geophys. Res.*, 120, 4263–4277.
- Aki, K. (1965). Maximum likelihood estimate of b in the formula $\log N = a - bM$ and its confidence limits. *Bull. Earthq. Res. Inst., Tokyo Univ.*, 43, 237-239.
- Baisch, S., Harjes, H.-P., 2003. A model for fluid-injection-induced seismicity at the KTB, Germany. *Geophys. J. Int.* 152, 160–170.
- Baisch, S., Vörös, R., Rothert, E., Stang, H., Jung, R., & Schellschmidt, R. (2010). A numerical model for fluid injection induced seismicity at Soultz-sous-Forêts. *International Journal of Rock Mechanics and Mining Sciences*, 47(3), 405-413.
- Baujard, C., Schoenball, M., Kohl, T., & Dorbath, L. (2014). Large magnitude events during injections in geothermal reservoirs and hydraulic energy: A heuristic approach. *Geothermics*, 52, 140-152.
- Bentz, S., Kwiatak, G., Martínez-Garzón, P., Bohnhoff, M., & Dresen, G. (2020). Seismic moment evolution during hydraulic stimulations. *Geophysical Research Letters*, 47(5), e2019GL086185.
- Berckmans, A. & Vandenberghe, N.: Use and potential of geothermal energy in Belgium, *Geothermics*, 27, (1998), 235-242.
- Beyreuther, M., Barsch, R., Krischer, L., Megies, T., Behr, Y., & Wassermann, J., 2010. Obspy: A python toolbox for seismology, *Seismological Research Letters*, 81(3), 530-533.
- Boore, D. M., & Boatwright, J. (1984). Average body-wave radiation coefficients. *Bulletin of the Seismological Society of America*, 74(5), 1615-1621.

- Bormann, P., & Dewey, J. W. (2012). The new IASPEI standards for determining magnitudes from digital data and their relation to classical magnitudes. In *New manual of seismological observatory practice 2 (NMSOP-2)* (pp. 1-44). Deutsches GeoForschungsZentrum GFZ.
- Bos, S., & Laenen, B. (2017). Development of the first deep geothermal doublet in the Campine Basin of Belgium. *European Geologist*, 43, 16-20.
- Bourouis, S., and P. Bernard (2007), Evidence for coupled seismic and aseismic fault slip during water injection in the geothermal site of Soultz (France), and implications for seismogenic transients, *Geophys. J. Int.* ,169(2),723–732.
- Broothaers, M., Lagrou, D., Harcouët-Menou, V. and Laenen, B. (2019) Lower Carboniferous limestone reservoir in northern Belgium: structural insights from the Balmatt project in Mol. *European Geothermal Congress 2019 Den Haag, The Netherlands, 11-14 June 2019.*
- Broothaers, M., Lagrou, D., Laenen, B., Harcouët-Menou, V. & Vos, D. (2021). Deep geothermal energy in the Lower Carboniferous carbonates of the Campine Basin, northern Belgium: An overview from the 1950's to 2020. *Z. Dt. Ges. Geowiss. (J. Appl. Reg. Geol.)*, 172 (3), 211-225.
- Brune, J. N. (1970). Tectonic stress and the spectra of seismic shear waves from earthquakes. *Journal of geophysical research*, 75(26), 4997-5009.
- Byerlee, J., 1978. Friction of Rocks. *Pure and applied geophysics* 116, 615-626.
[dx.doi.org/10.1007/BF00876528](https://doi.org/10.1007/BF00876528).
- Cao, A. M., and S. S. Gao (2002), Temporal variations of seismic b-values beneath northeastern japan island arc, *Geophys. Res. Lett.*, 29, doi:10.1029/2001GL013775.
- Cauchie, L., Lengliné, O., & Schmittbuhl, J. (2020). Seismic asperity size evolution during fluid injection: case study of the 1993 Soultz-sous-Forêts injection. *Geophysical Journal International*, 221(2), 968-980.
- Contrucci, I., Klein, E., Bigarre, P., Lizeur, A., Lomax, A., & Bennani, M. (2010). Management of post-mining large-scale ground failures: blast swarms field experiment for calibration of permanent microseismic early-warning systems. *Pure and applied geophysics*, 167(1), 43-62.
- Cornet, F. H., Helm, J., Poitrenaud, H., & Etchecopar, A. (1997). Seismic and aseismic slips induced by large-scale fluid injections. In *Seismicity associated with mines, reservoirs and fluid injections* (pp. 563-583). Birkhäuser, Basel.
- Cornet, F. H. (2016). Seismic and aseismic motions generated by fluid injections. *Geomechanics for Energy and the Environment*, 5, 42-54.
- Cotton, F, and Coutant O., (1997), Dynamic stress variations due to shear faults in a plane-layered medium, *GJI*, Vol 128, 676-688

Coutant, O. (1990), Programme de Simulation numérique AXITRA, Rapport LGIT, Université Joseph Fourier, Grenoble, France.

De Barros, L., Daniel, G., Guglielmi, Y., Rivet, D., Caron, H., Payre, X., ... & Gourlay, M. (2016). Fault structure, stress, or pressure control of the seismicity in shale? Insights from a controlled experiment of fluid-induced fault reactivation. *Journal of Geophysical Research: Solid Earth*, 121(6), 4506-4522.

De Barros, L., Cappa, F., Guglielmi, Y., Duboeuf, L., & Grasso, J. R. (2019). Energy of injection-induced seismicity predicted from in-situ experiments. *Scientific reports*, 9(1), 1-11

De Santis, F., Contrucci, I., Kinscher, J., Bernard, P., Renaud, V. & Gunzburger, Y., 2019. Impact of geological heterogeneities on induced seismicity in a deep sublevel stoping mine, *Pure appl. Geophys.*, 176(2), 697–717.

Duboeuf, L., De Barros, L., Cappa, F., Guglielmi, Y., Deschamps, A., & Seguy, S. (2017). Aseismic motions drive a sparse seismicity during fluid injections into a fractured zone in a carbonate reservoir. *Journal of Geophysical Research: Solid Earth*, 122(10), 8285-8304.

Duverger, C., Lambotte, S., Bernard, P., Lyon-Caen, H., Deschamps, A., & Necessian, A. (2018). Dynamics of microseismicity and its relationship with the active structures in the western Corinth Rift (Greece). *Geophysical Journal International*, 215(1), 196-221.

Gaucher, E., Schoenball, M., Heidbach, O., Zang, A., Fokker, P. A., van Wees, J. D., & Kohl, T. (2015). Induced seismicity in geothermal reservoirs: A review of forecasting approaches. *Renewable and Sustainable Energy Reviews*, 52, 1473-1490.

Galis, M., Ampuero, J. P., Mai, P. M., & Cappa, F. (2017). Induced seismicity provides insight into why earthquake ruptures stop. *Science advances*, 3(12), eaap7528.

GEOHEAT-APP (2014). Economic feasibility of intermediate and deep geothermal energy in supplying sustainable heat for building and renovation projects. VITO, Grontmij-Nederland & TNO, Interreg Vlaanderen-Nederland. <https://vito.be/nl/geoheat-app>

Giardini, D. (2009). Geothermal quake risks must be faced. *Nature*, 462 (7275), 848–849.

Guglielmi, Y., Cappa, F., Avouac, J. P., Henry, P., & Elsworth, D. (2015). Seismicity triggered by fluid injection–induced aseismic slip. *Science*, 348(6240), 1224-1226.

Hallo, M., Oprsal, I., Eisner, L., & Ali, M. Y. (2014). Prediction of magnitude of the largest potentially induced seismic event. *Journal of Seismology*, 18(3), 421-431.

Hanks, T. C., & Kanamori, H. (1979). A moment magnitude scale. *Journal of Geophysical Research: Solid Earth*, 84(B5), 2348-2350.

Häring, M. O., Schanz, U., Ladner, F., & Dyer, B. C. (2008). Characterisation of the Basel 1 enhanced geothermal system. *Geothermics*, 37(5), 469-495.

- Hopp, C., Sewell, S., Mroczek, S., Savage, M., & Townend, J. (2019). Seismic response to injection well stimulation in a high-temperature, high-permeability reservoir. *Geochemistry, Geophysics, Geosystems*, 20(6), 2848-2871.
- Huang, Y., Ellsworth, W. L., & Beroza, G. C. (2017). Stress drops of induced and tectonic earthquakes in the central United States are indistinguishable. *Science advances*, 3(8), e1700772.
- Huang, Y., De Barros, L., & Cappa, F. (2019). Illuminating the rupturing of microseismic sources in an injection-induced earthquake experiment. *Geophysical Research Letters*, 46(16), 9563-9572.
- Huenges, E., & Ledru, P. (Eds.). (2011). *Geothermal energy systems: exploration, development, and utilization*. John Wiley & Sons.
- Ide, S., G. C. Beroza, S. G. Prejean, and W. L. Ellsworth (2003), Apparent break in earthquake scaling due to path and site effects on deep borehole recordings, *J. Geophys. Res.*, 108(B5), 2271, doi:10.1029/2001JB001617.
- Jeanne, P., Rutqvist, J., Rinaldi, A. P., Dobson, P. F., Walters, M., Hartline, C., & Garcia, J. (2015). Seismic and aseismic deformations and impact on reservoir permeability: The case of EGS stimulation at The Geysers, California, USA. *Journal of Geophysical Research: Solid Earth*, 120(11), 7863-7882.
- Kinscher, J., Cesca, S., Bernard, P., Contrucci, I., Mangeney, A., Pigué, J.P. & Bigarre, P., 2016. Resolving source mechanisms of microseismic swarms induced by solution mining, *Geophys. J. Int.*, 206(1), 696–715.
- Kinscher, J. L., De Santis, F., Poiata, N., Bernard, P., Palgunadi, K. H., & Contrucci, I. (2020). Seismic repeaters linked to weak rock-mass creep in deep excavation mining. *Geophysical Journal International*, 222(1), 110-131.
- Kinscher, J.L., (2020). Seismic hazard and risk analysis at Balmatt Part2: Characterization of the triggering mechanism, hazard and risk assessment. Ineris Report (ref. Ineris-200066-2045899).
- Kluge, C., Blöcher, G., Hofmann, H., Barnhoorn, A., Schmittbuhl, J., & Bruhn, D. (2021). The stress-memory effect of fracture stiffness during cyclic loading in low-permeability sandstone. *Journal of Geophysical Research: Solid Earth*, 126, e2020JB021469. <https://doi.org/10.1029/2020JB021469>
- Konstantinovskaya, E., Malo, M., & Castillo, D. A. (2012). Present-day stress analysis of the St. Lawrence Lowlands sedimentary basin (Canada) and implications for caprock integrity during CO₂ injection operations. *Tectonophysics*, 518, 119-137.
- Kwiatak, G., Martínez-Garzón, P., Dresen, G., Bohnhoff, M., Sone, H., & Hartline, C. (2015). Effects of long-term fluid injection on induced seismicity parameters and maximum magnitude in northwestern part of The Geysers geothermal field. *Journal of Geophysical Research: Solid Earth*, 120(10), 7085-7101.

- Kwiatek, G., Saarno, T., Ader, T., Bluemle, F., Bohnhoff, M., Chendorain, M., ... & Leonhardt, M. (2019). Controlling fluid-induced seismicity during a 6.1-km-deep geothermal stimulation in Finland. *Science advances*, 5(5), eaav7224.
- Lecocq, T. and Camelbeeck, T. (2017) Report of Royal Observatory of Belgium on the seismic activity recorded during the injection tests. *Induced Seismic Activity at the Balmatt-site*.
- Lee, K.-K., Ellsworth, W.L., Giardini, D., Townend, J., Ge, S., Shimamoto, T., Yeo, I.-W., Kang, T.-S., Rhie, J., Sheen, D.-H., 2019. Managing injection-induced seismic risks. *Science* 364, 730–732.
- Lengliné, O., L. Lamourette, L. Vivin, N. Cuenot, and J. Schmittbuhl (2014), Fluid-induced earthquakes with variable stress drop, *J. Geophys. Res. Solid Earth*, 119, 8900–8913.
- Lengliné, O., Boubacar, M., & Schmittbuhl, J. (2017). Seismicity related to the hydraulic stimulation of GRT1, Rittershoffen, France. *Geophysical Journal International*, 208(3), 1704-1715.
- Madariaga, R. (1976). Dynamics of an expanding circular fault. *Bulletin of the Seismological Society of America*, 66(3), 639-666.
- McGarr, A. (2014). Maximum magnitude earthquakes induced by fluid injection. *Journal of Geophysical Research: solid earth*, 119(2), 1008-1019.
- McGarr, A., & Barbour, A. J. (2018). Injection-induced moment release can also be aseismic. *Geophysical Research Letters*, 45(11), 5344-5351.
- Mignan, A., Broccardo, M., Wiemer, S., Giardini, D., 2017. Induced seismicity closed-form traffic light system for actuarial decision-making during deep fluid injections. *Scientific reports* 7, 13607.
- Moeck, I., Bloch, T., Graf, R., Heuberger, S., Kuhn, P., Naef, H., Sonderegger, M., Uhlig, S., Wolfgramm, M., 2015. The St. Gallen project: development of fault controlled geothermal systems in urban areas, in: *Proceedings World Geothermal Congress*. pp. 1–5.
- Ogata, Y., & Katsura, K. (1993). Analysis of temporal and spatial heterogeneity of magnitude frequency distribution inferred from earthquake catalogues. *Geophysical Journal International*, 113(3), 727-738.
- Orlecka-Sikora, B., & Cielesta, S. (2020). Evidence for subcritical rupture of injection-induced earthquakes. *Scientific Reports*, 10(1), 1-15.
- Schmittbuhl, J., Lambotte, S., Lengliné, O., Grunberg, M., Jund, H., Vergne, J., ... & Masson, F. (2021). Induced and triggered seismicity below the city of Strasbourg, France from November 2019 to January 2021. *Comptes Rendus. Géoscience*, 353(S1), 561-584.
- Shanks, D. 1993 *Solved and Unsolved Problems in Number Theory*, 4th ed. New York: Chelsea, pp. 56-57.

- Shapiro, S. A., Dinske, C., & Kummerow, J. (2007). Probability of a given-magnitude earthquake induced by a fluid injection. *Geophysical research letters*, 34(22).
- Shapiro, S. A., Dinske, C., Langenbruch, C., & Wenzel, F. (2010). Seismogenic index and magnitude probability of earthquakes induced during reservoir fluid stimulations. *The Leading Edge*, 29(3), 304-309.
- Shapiro, S. A., Krüger, O. S., Dinske, C., & Langenbruch, C. (2011). Magnitudes of induced earthquakes and geometric scales of fluid-stimulated rock volumes. *Geophysics*, 76(6), WC55-WC63.
- Uchida, N. and R. Burgmann (2019). Repeating earthquakes, *Annu. Rev. Earth Planet. Sci.*, 47(1), 305-332.
- Van der Elst, N. J., Page, M. T., Weiser, D. A., Goebel, T. H., & Hosseini, S. M. (2016). Induced earthquake magnitudes are as large as (statistically) expected. *Journal of Geophysical Research: Solid Earth*, 121(6), 4575-4590.
- Vandenberghe, N., 1991: Belgium. - In: *Geothermal Atlas of Europe* (Eds.: Hurtig, E., Cermak, V., Haenel, R. and Zui, V.), Hermann Haack Verlagsgesellschaft, Gotha, Germany, p. 14-15
- Vandenberghe, N. and Bouckaert, J. (1980). Geologische aspecten van de mogelijkheid tot de aanwending van geothermische energie in Noord België. Geological Survey of Belgium. Professional Paper, 168, 1-34.
- Vanneste, K., Lecocq, T., Van Camp, M. and Camelbeeck, T. (2019) Report of Royal Observatory of Belgium Report ROB-SCK 2019-01 version 1 and ROB-SCK 2019-02 v. 2 on Evaluation of the impact of induced seismicity by the Balmatt geothermal plant at the SCK-CEN Nuclear Research Centre: Calculation of acceleration response spectra and moment magnitude of the largest induced events.
- Wang, H. F. (2000). *Theory of Linear Poroelasticity*, Princeton Ser. Geophys.
- Waldhauser, F., and W. L. Ellsworth (2000), A double-difference earthquake location algorithm: Method and application to the northern Hayward fault, California, *Bull. Seismol. Soc. Am.*, 90(6), 1353–1368.
- Wei, S., Avouac, J. P., Hudnut, K. W., Donnellan, A., Parker, J. W., Graves, R. W., ... & Eneva, M. (2015). The 2012 Brawley swarm triggered by injection-induced aseismic slip. *Earth and Planetary Science Letters*, 422, 115-125.
- Wenzel, F. (2017). Fluid-induced seismicity: comparison of rate- and state- and critical pressure theory. *Geothermal Energy*, 5(1), 1-16.
- Wiemer, S., and M. Wyss (2000), Minimum magnitude of complete reporting in earthquake catalogs: examples from alaska, the western united states, and japan, *Bull. Seismol. Soc. Am.*, 90, 859–869.

Wynants-Morel, N., Cappa, F., De Barros, L., & Ampuero, J. P. (2020). Stress perturbation from aseismic slip drives the seismic front during fluid injection in a permeable fault. *Journal of Geophysical Research: Solid Earth*, 125(7), e2019JB019179.

Zang, A., Stephansson, O., Heidbach, O., & Janouschkowetz, S. (2012). World stress map database as a resource for rock mechanics and rock engineering. *Geotechnical and Geological Engineering*, 30(3), 625-646.

Zang, A., Oye, V., Jousset, P., Deichmann, N., Gritto, R., McGarr, A., ... & Bruhn, D. (2014). Analysis of induced seismicity in geothermal reservoirs—An overview. *Geothermics*, 52, 6-21.

Zoback, M. D., Barton, C. A., Brudy, M., Castillo, D. A., Finkbeiner, T., Grollimund, B. R., ... & Wiprut, D. J. (2003). Determination of stress orientation and magnitude in deep wells. *International Journal of Rock Mechanics and Mining Sciences*, 40(7-8), 1049-1076.

Appendix A: Search for seismic events located at the injection well during stimulation tests in September 2016

As stated in 3.2 and 4.2, seismicity in P1-P3 seemed to be absent in the direct vicinity of the injection well. In the following analysis we try to clarify whether seismicity during the preceding test phases in 2016 differs to that during P1-P3. If this is the case, the difference might be related to a location closer to the injection well. As introduced in Section 2.2, seismic monitoring during the injection tests on 14-16 September 2016 was limited to only two stations, namely DSLB and MOLT. The seismic catalogue during this experiment was mainly generated by means of template matching based detection which resulted in the identification of around 300 events whose locations and magnitudes could be only approximated on a first order (Lecocq and Camelbeeck, 2017). Magnitudes ranged generally between -2.0 and almost 1.0 meanwhile the strongest event occurred around 16.5 days after shut-in. Clustering analysis by means of cross-correlation based wave form comparison demonstrated high similarity between most of the events which were classified in around four main multiplet groups.

In order to check for similarity and dissimilarity between events in 2016 and during P1-P3 injection phases we calculated the cross-correlations for the wave forms of all the three components of stations DSLB and MOLT for all possible event pairs. For each event in 2016 we calculated then the maximum correlation coefficient with respect to any event in P1-P3 as shown in Figure C.1a. Interestingly, the results showed that the seismic events recorded during the first 10 hours of the stimulation phase in September 2016 are systematically more dissimilar in waveforms to the seismic events in P1-P3. Moreover, the four main multiplet families in 2016 (first appearing after the 10 hours initial phase) were found to be exactly the same families 1 - 4 that we identified in P1 (Figure 7).

To highlight a possible difference in location of the dissimilar events in 2016, we manually picked the arrival times of P and S wave phase t_p and t_s at each station for all 2016 events. In the results, as shown in Figure C1c-d, we found a comparatively larger t_s-t_p travel time difference at both stations for the dissimilar event group which would be a priori consistent with a location at the injection well. Moreover, magnitudes for these events seem to be generally smaller compared to those for later events (Figure C1b). From these results we suggest that the dissimilar events may potentially be related to the opening of smaller fractures close to the

injection well due to the strong pore pressure perturbations and potential fracture opening (Section 4.2). However, the systematic smaller event magnitude may also bias our findings in Figure C1a since they also imply lower signal-to-noise ratios and consequently systematic smaller correlation coefficients.

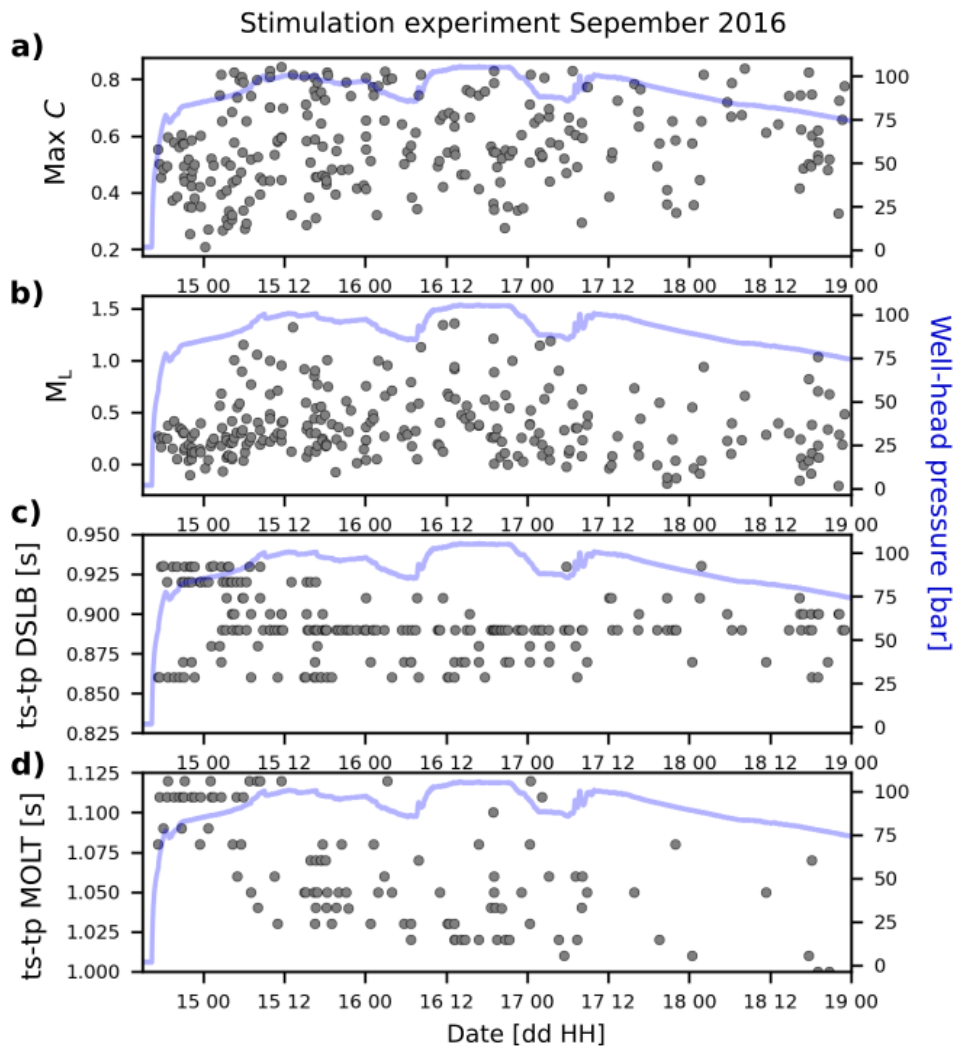


Figure A1: Results from waveform comparison and characterisation for September 2016 stimulation experiment (see text).

Appendix B Evaluation of reliability of distant event location to the injection point

To evaluate the quality of the velocity model and source location results, we first inspected the qualitative fit of observed P and S wave phases in seismograms with theoretical arrival times related to the obtained maximum likelihood source location. As shown as an example by the Jan-M1.8-event in Figure B1a, all theoretic arrival times are in very good agreement with seismogram phases when considering locations westward of the injection well. In contrast, a clear degradation in the fit is seen when assuming a location at the injection well. Quantitative estimation of the respective misfits has shown that this degradation corresponds to an increase in the root mean square error (RMS) of around 400%. These results indicate that the chosen 1D velocity model is an appropriate choice to explain observed P and S wave arrivals and that major 3D velocity effects can be widely excluded. Absence of potential stronger lateral velocity variations is furthermore supported by generally stable and consistent P wave velocities observed at different well logs located around the project site (Figure 1b and Figure 4b).

Secondly, we assessed the spatial distribution of location errors related to the uncertainty of observed P and S wave arrival time picks by visualizing the cumulative probability density function (PDF) for the Jan-M1.8-event in Figure B1b. We find that there is a chance of 99% (0.99 contour of the PDF) that the event is located at least several hundred meters west of the injection well. Furthermore, back azimuth angles estimated from P wave polarization at station DSLNZ seem clearly better in agreement with a location westward of the injection well. Sensor orientation of DSLNZ station was previously derived by means of active vibroseis sources used during a VSP survey at GT-03. Following these observations, it appears thus likely (even though not 100%) that most of the seismic events occur at some hundred-meter distance to the injection well.

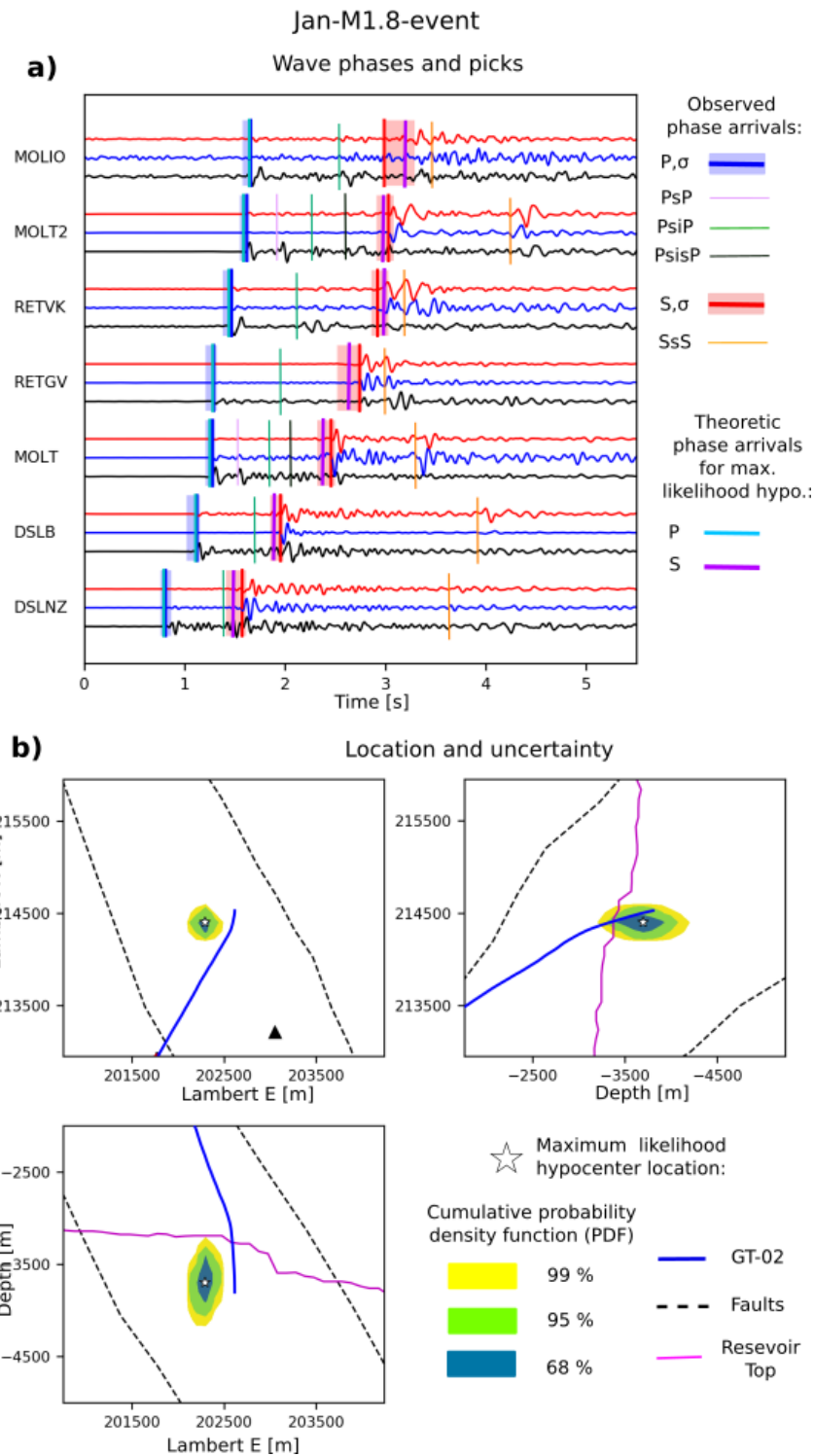


Figure B1: P and S wave phase picking and location uncertainty for the Jan-M1.8-event. a) Direct P and S wave phases picked from seismograms (blue and red lines) and theoretically predicted (cyan and magenta lines) from the velocity model (Figure 4b) using AXITRA code, 50

corresponding to the maximum likelihood hypocentre location of the event shown in b). Other coloured lines show observed multiple reflection phases as illustrated in Figure 4c. b) The spatial location error as related to the uncertainties of P and S waves arrival time picks σ shown in a) (blue and red shaded areas) and the velocity model of Figure 4b expressed by the cumulative probability density function.

Appendix C: Complement to multiplet analysis

C.1 Clustering analysis

Clustering analysis was based on the calculation of the cross-correlation coefficient C . We used waveforms of the entire seismograms filtered at 10 - 50 Hz for all three components Z, N, E of station MOL2A for all event pairs for the total of the 267 events (Section 2). The choice of using only the most distant station is justified by the fact that MOL2A provides high event detection capacity (Section 2.3) and was operational over the entire monitoring period from December 2018 to October 2019 (DSL2B and MOLT were only operational during P1 and P2).

The resulting correlation matrix of the applied approach is shown in Figure C1a. We notice generally high similarities between most of the events. More than 80 % of the events show similarities characterized with $C > 0.7$, and $C > 0.9$ is observed for more than 30 % (Figure C1c). High similarity is also often observed for event pairs with very different origin times (up to six months) (Figure C1b). These observations agree with the result from absolute locations indicating strong spatial and persistent clustering over the entire production period. In addition, two main event clusters, as seen from absolute event locations, are also visible in the correlation matrix while also some sub-clusters can be suggested from higher correlation coefficients for certain event pairs (Figure C1a).

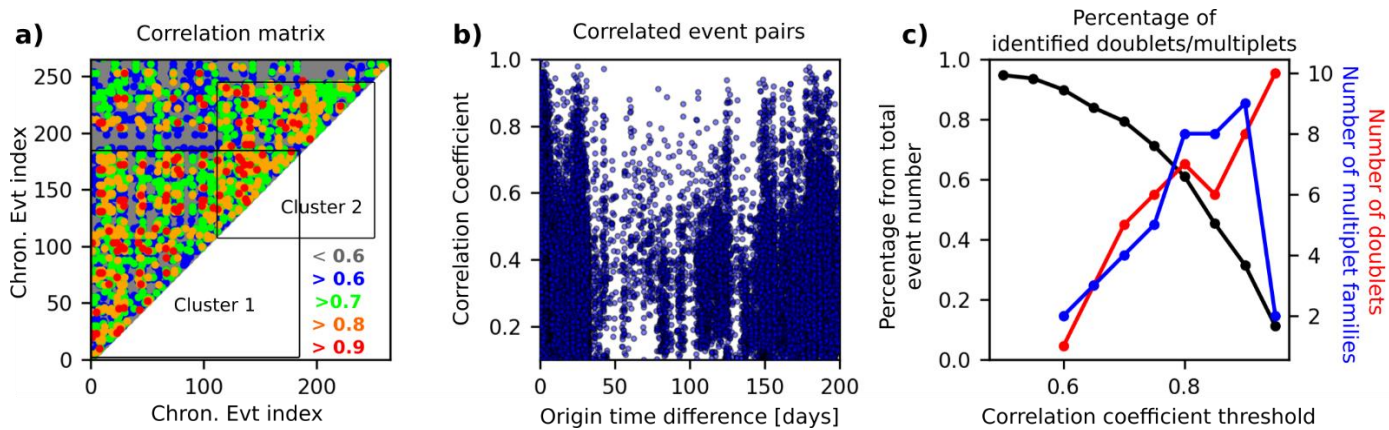


Figure C1: Cross-correlation analysis for all event pairs of the 267 recorded events using station MOL2. a) The cross-correlation matrix confirming the presence of two main event clusters in agreement with two clusters seen from absolute location results (Figure 5); b) cross-correlation coefficients of event pairs as a function of their difference in origin time ;c) Percentage of total number of identified doublets and multiplet events (black curve) and classified families (red and blue curve, respectively) as a function of different correlation-coefficient thresholds.

C.2 Relocation

In the here performed relocation approach, we take advantage of high similarity in waveforms which allows estimating very precise time delays for P and S arrivals for different multiplet event pairs using cross-correlation. Cross-correlation was performed by windowing (0.5 s) the direct P and S wave phases separately after filtering seismograms at 10-50 Hz. These detailed delays were then interpreted as relative locations between events with respect to the family's centroid by using the double difference method of Waldhauser and Ellsworth (2000), i.e., analysing the differential arrival times of P and S wave for different event pairs and station couples. A weighting function has been used to privilege double-difference arrival times associated with high C . Differential arrival times estimated with $C < 0.65$ have been excluded and only events were considered that have been recorded by at least three stations.

Relocation performance is strongly limited by station DSLNZ (Section 2.3). As a result, most low magnitude events, which are mainly present in families 2, 3, 7 and 8, have significant errors

(several hundred meters) in absolute and relative locations and need to be considered with caution. Best data quality was observed for family 1 dominated by stronger events ($M_L > 0.5$).

Appendix D Approximation of source parameters

To examine spatial source dimensions and to derive stress drops for the recorded events, we determined the moment magnitude (M_w) linked to the seismic moment M_0 (Hanks and Kanamori, 1979) and the corner frequency (f_c) by using the displacement (expressed in moment magnitude) source spectrum approach by De Santis et al. (2019), Cauchie et al. (2020) and Kinscher et al. (2020). In this approach the observed source spectra of S waves are fitted to a classical Brune's model (Brune, 1970) combined with an anelastic attenuation term by applying a (spectral signal to noise ratio based weighted) grid search over M_w , f_c and the Q factor. In the solution space we look for a common M_w and a common f_c while Q is individually estimated for each station (ranging from 100-1000), which is expected since each station is located at different depth. In this way we try to reduce the bias from differences in Green functions on corner frequency estimates (e.g., Abercrombie, 2015; Ide et al., 2003;).

The computation has been performed using signals of stations DSLNZ, MOLT and MOL2A only, which presented overall better data quality than near surface stations RETVK and RETGV. Due to its limited availability, data of station DSLB has been excluded here in order to avoid potential bias in the results related to variable input data. As a homogeneous propagation model was used to account for attenuation, we used higher S-wave velocities V_s for DSLNZ (2200 m/s) than for MOL2A and MOL4 (2000 m/s) which correspond to the rough average velocities when assuming only the vertical direct source-station wave paths (for a source located at the reservoir top) and the velocity model of Section 3.1. This average calculation implies an overestimation of the attenuation effect (especially for station MOL2 and MOL4) since seismic ray paths are in fact travelling longer in deeper high-speed layers for larger epicentral distance. Nonetheless, we must remind here that our approach does not account for scattering effects related to the strong velocity contrast (especially at 600 m) such that our approach must be considered a first order approximation only. Other relevant parameters used were the average radiation coefficient for S-waves $R_s = 0.6$ (Boore and Boatwright, 1984) and an average density ρ assumed to be equal to 2700 kg/m³.

Observed source spectra have been visually inspected and noisy events have been rejected resulting in a total of 57 analysed events (only ~ 21% of the total data set) from which the large majority has been classified as multiplets (only 4 singlets). Once again, it must be noted that the number of analysed events was generally low due to the low detectability at station DSLNZ (Section 2.3), which was considered essential for the analysis (since probably most sensitive to differences in corner frequencies). Results show that M_W ranges between 0.5 and 2.0 and f_c between 4 Hz and 23 Hz, which corresponds to source radii around 11 m - 68 m using Madariaga (1976) model and assuming a rupture velocity of 2.9 km/s (Figure b). These results agree with previous investigations on corner frequency using a similar source spectrum fit and a spectral ratio approach by Vanneste et al. (2019).

As shown by Figure D1, stress drops are in the range of 0.1 – 10 MPa which seems rather low as compared to natural earthquakes mostly in the order of 1 - 100 MPa (e.g., Huang et al., 2017). Interestingly, source radii seem to be very similar for most events (and for each multiplet family) while the seismic moment and stress drop vary by more than a factor 100 as similarly observed by Lengliné et al., (2014) and Cauchie et al. (2020) for the Soultz-sous-Forêts site. Relatively high stress drops are observed for the largest events, namely the Jan-M1.8-event and the Jun-M2.2-event being close to 10 MPa. We remind here that these results should be seen as first order approximations only, especially due to the limited station number, frequency band and the influence of attenuation effects (e.g. potential trade-off of Q and f_c) which were not very well approximated by our approach. Nonetheless, we believe that significant stress drop variations for different multiplet families are a reliable result even though absolute values should be regarded with caution here. Qualitative evidence for strong stress drop variation is given from similarity of the source spectra of station DSLNZ as shown for family 1 in Figure D1a, which show a very similar corner frequency while the spectral plateau changes over more than one order of Magnitude.

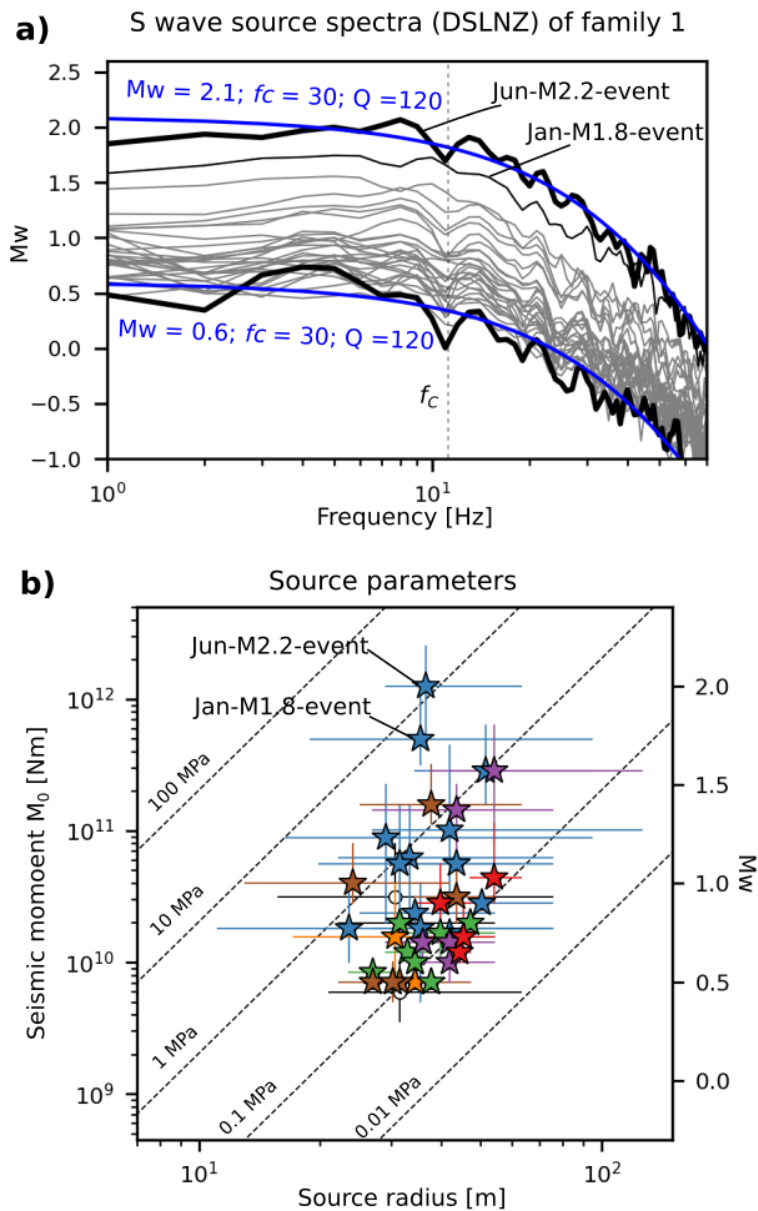


Figure D1 Results from source parameters estimated for a total of 57 events. a) Example of source spectra for multiplets of family 1 expressed in moment magnitude M_w . Note the general similarity in corner frequencies f_c despite significant changes in magnitude as illustrated for the example of the Jun-M2.2-event and a very similar but significantly smaller event (thick black lines). The respective fitted synthetic source spectra are shown too (blue lines); b) stress drops shown for multiplets (stars with colour code as defined in Figure 7) and singlets and doublets (white circles).

Appendix E Source mechanisms

E.1 Method description

Source mechanism analysis was done by means of a full waveform inversion approach following Kinscher et al. (2016, 2020) by fitting synthetic (Coutant, 1990) and observed full seismograms (including P and S waves) in the time domain, using a classical shear dislocation model represented by double-coupled body forces. A grid search was used to invert for moment magnitude (0 – 3) with 0.1 intervals and strike (0 – 360°), dip (0 – 90°) and rake (0 – 360°) with 10° intervals. Observed and synthetic waves were filtered at 0.6 – 3 Hz (except group 2 at 1 – 10 Hz, Table 1) and fitted by using the L2 norm. In order to avoid phase shifts related to uncertainty in the calculated Green functions (velocity model), waveforms were aligned using cross-correlation. Instrumental response had to be corrected for stations DSLNZ and MOL2A being short-period sensors (2 Hz), which has been achieved by multiplying the inverse transfer function in the spectral domain. Highest station coverage was available for MECA 1 including the Jan-M1.8-event (Table 1).

E.2 Comparison of source mechanism solutions to P wave polarity

Solutions obtained from wave form inversion are compared to P wave polarities and relative attenuation corrected amplitudes in Figure E1. P wave polarities were estimated from first movement of the P wave arrival in the Z components and projected into the lower source hemisphere (beachball) by calculating the station backazimuth and take-off angle based on the evaluated velocity model and provided source location (Section 3.1 and 3.2). We observe that strike-slip solutions from wave form inversion and polarities are in very good agreement, i.e. positive polarities are observed in the compressive quadrants (lobes) and negative polarities in the dilative quadrants of the focal mechanism sphere. Also, relative P wave amplitude generally agrees with the P wave radiation pattern associated with a maximum amplitude normal to each nodal plane. A particular case is represented by the closest station DSLNZ which shows comparatively small P wave amplitudes and varying polarities for different events. Also, this particular polarity behaviour agrees very well with the obtained solution since such variability in polarity and small amplitude is expected when the station is located at one or at the intersection of the nodal planes.

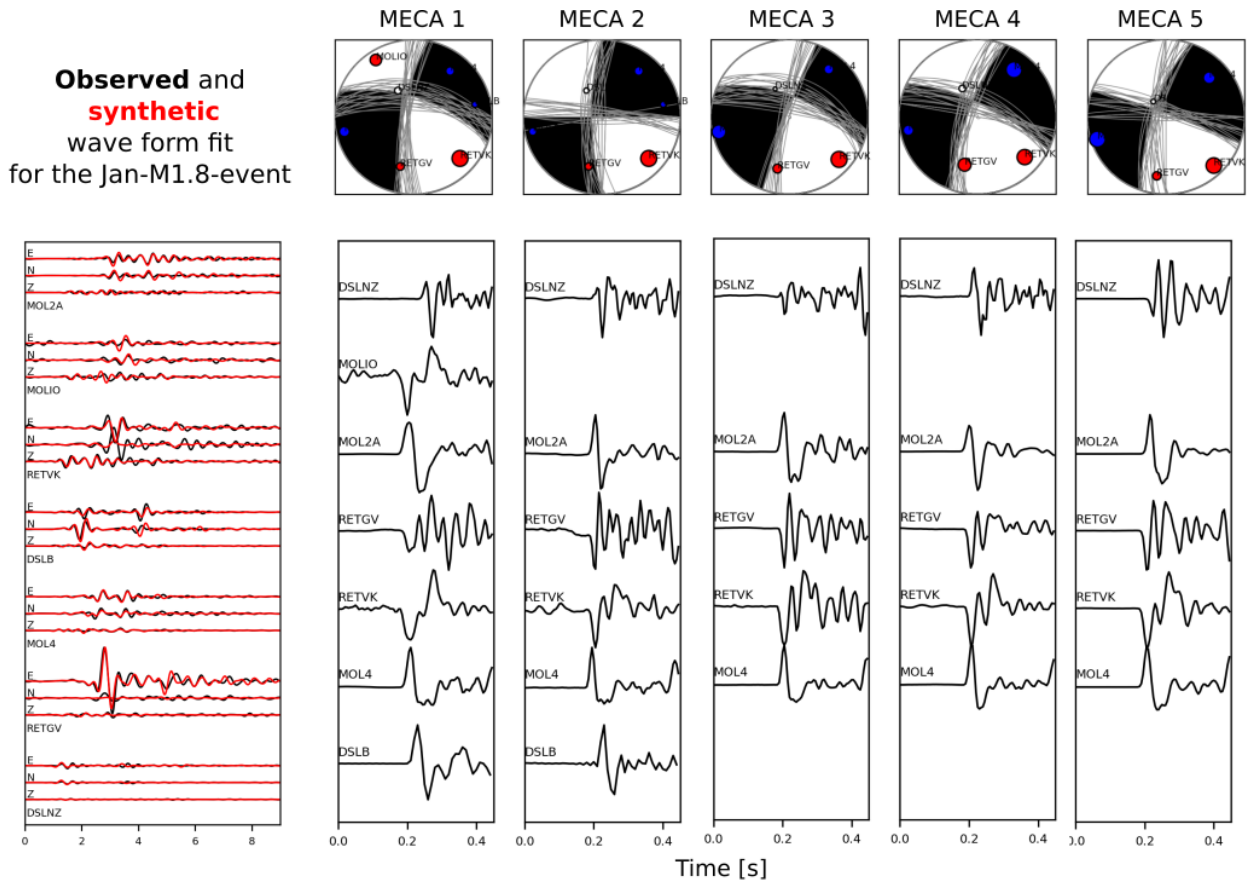


Figure E1 Comparison between source mechanism obtained from wave form inversion (Table 1) and polarities of the first P wave movement. (left) comparison of observed (black) and synthetic (red) wave of forms for MECA 1; (right) beach balls for each group (colours and columns) represent the source mechanisms obtained from minimum misfit from wave form inversion while grey lines represent the nodal planes for the best fitting 25 solutions. Positive (blue points) and negative (red point) P wave polarities are plotted into the lower source hemisphere (beachball) for each station. The size of the polarities (points) corresponds to the P wave amplitude relative between all stations corrected for attenuation (multiplication by hypocentral distance). (below) all available wave forms for the first P wave movement.

E.3 Solution space and sensitivity tests

Distribution of the misfit in the parameter space (strike, dip, rake) demonstrates clearly that inversion is converging with continuously decreasing misfit towards the optimal solution (Figure 57

E2). Sensitivity of inversion results was further investigated with respect to source depth and epicentre location, which both are affected by uncertainty and may influence the result. Our analysis shows that changes in source depth do not significantly change the source mechanism solutions. Misfits become slightly smaller when assuming source depths around 3250 – 3500 m, which agrees with depths found from body wave phase picking based locations. In addition, source mechanism solutions appear generally stable when allowing for ~ 500 m shifts from the initial epicentre location which demonstrates that obtained results are generally robust to epicentre location uncertainty.

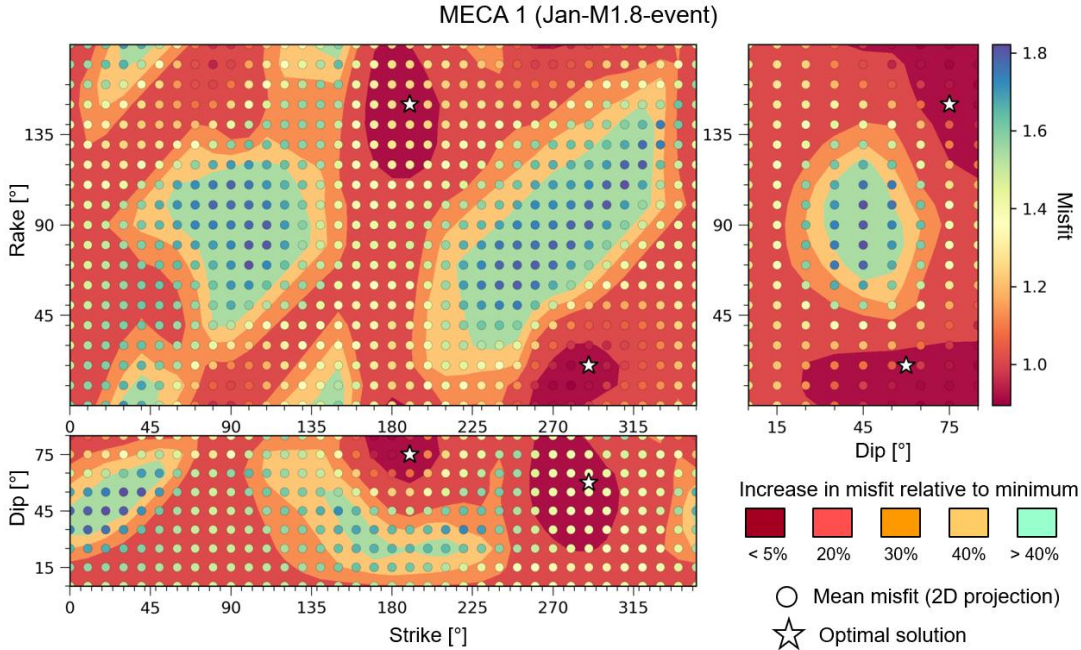


Figure E2 Solution space for source mechanisms inversion for the Jan-M1.8-event.